Fracture-Induced Anisotropy of the Stress-Strain Response of Shale at Multiple Scales

Hao Xu[1], Seth Busetti, [2] and Chloé Arson[3],

ABSTRACT

This paper investigates deformation and stiffness anisotropy induced by damage propagation in rock brittle deformation regime. Specifically, a Finite Element-based Continuum Damage Mechanics model is used to capture sample size effects and the influence of intrinsic anisotropy on the stress-strain response of shale. The Differential Stress Induced Damage (DSID) model previously proposed by the authors is calibrated against triaxial compression tests performed on North Dakota Bakken shale samples. Laboratory tests simulated with the Finite Element Method reproduce deformation and damage localization phenomena, and capture the increase of boundary effects expected in larger samples. Simulations performed for various initial states of damage are used to investigate the role of the dominant fabric anisotropy of the rock: bedding planes in shale are modeled by a smeared damage zone with the DSID model and by a discrete crack plane. The continuum approach successfully captures the development of microcrack propagation and energy dissipation at the early stage of the strain hardening process observed in triaxial compression tests. Additionally, using initial anisotropic damage can effectively account for various types of mechanical anisotropy in shale.

Keywords: Shale, Anisotropy, Continuum Damage Mechanics, Finite Element Method

INTRODUCTION

Shale is a sedimentary rock that naturally exhibits discontinuities at multiple scales, for exam-

[1]School of Civil and Environmental Engineering, Georgia Institute of Technology, Atlanta, Georgia 30332, USA. Current address: Energy Geosciences Division, Earth & Environmental Sciences Area, Lawrence Berkeley National Laboratory, Berkeley, CA 94720, USA. E-mail: haoxu@lbl.gov.

[2]Structure & Geomechanics Group, ConocoPhillips, Houston, Texas 77079, USA. E-mail: seth.busetti@conocophillips.com

[3]School of Civil and Environmental Engineering, Georgia Institute of Technology, Atlanta, Georgia 30332, USA. E-mail: chloe.arson@ce.gatech.edu. Corresponding author.

ple: grain-scale contacts, brittle microcracks, fine laminations, through-going natural fractures and faults, and bedding contacts and layering. Modeling the interaction between these discontinuities presents theoretical and numerical challenges. The main strategies available are based on fracture mechanics, damage mechanics and fluid mechanics (e.g., lubrication theory).

Fractures involved in the fracturing process can occur at any scale, ranging from microcracks initiated under the influence of a differential stress, e.g. the Griffith cracks following Linear Elastic Fracture Mechanics (LEFM, referred to as "microscale" in the following, e.g., (Bahat et al. 2005)), to macroscopic natural fractures of geologic origin that propagate within reservoirs (referred to as "macroscale" in the following, e.g., (Nelson 2001)). Several numerical methods may be employed in LEFM (Mohammadi 2007), mainly the Finite Element Method (FEM), the Extended Finite Element Method (XFEM), Cohesive Zone Models (CZM) (Carrier and Granet 2012) and Boundary Element Methods (BEM) (Elleithy et al. 2001; Raveendra and Cruse 2005). In all of these methods however, fracture nucleation and intersection are impossible to predict, and the position and starting geometry of the fracture must be pre-determined. Stress intensity factors were used to predict the movement of fracture tips (Savitski and Detournay 2002), but the weakening of the solid part of the rock was not taken into account. In Continuum Damage Mechanics (CDM), subsets of cracks are defined as "damage", a quantity that relates to the amount of stiffness and/or strength degradation observed during deformation (Lemaître and Desmorat 2005; Krajcinovic 1996). Phenomenological CDM models are based on a minimum of two postulates: the expression of the free energy of the solid skeleton of the porous rock, and the expression of a dissipation potential (Arson and Gatmiri 2008). Damaged poro-elastic properties (Homand-Etienne et al. 1998; Shao 1998; Shao and Lydzba 1999; Swoboda et al. 1995; Swoboda et al. 1997; Swoboda and Yang 1999b; Dufour et al. 2012; Xu and Arson 2014; Zhu and Arson 2014) and damaged permeability (Shao et al. 2005; Zhou et al. 2006; Arson and Pereira 2013; Pereira and Arson 2013) are computed from purely energetic considerations, by evaluating the dissipation associated to crack softening and irreversible crack opening. The choice of dissipation variables (e.g., damage variable(s) and inelastic strain(s)) is a key point in the modeling approach (Arson et al. 2012; Arson

2014). In micro-mechanical CDM models (Dormieux et al. 2006), the main challenge consists in describing the set of cracks present in the medium, by gathering them according to their size and orientation (Swoboda and Yang 1999a). Within each set, crack growth is generally controlled by a Griffith criterion. The damaged stiffness tensor is calculated with the updated crack geometry in an appropriate homogenization scheme (e.g. the self-consistent method or Mori-Tanaka scheme). Micro-mechanical damage models have successfully been extended to saturated porous media in order to predict damaged poro-elastic properties (e.g. stiffness and Biot tensors) (Deudé et al. 2002b; Deudé et al. 2002a; Lydzba and Shao 2000; Xie et al. 2012; Lu and Elsworth 2012) and damaged permeability (Kondo and Dormieux 2004; Maleki and Pouya 2010).

Because specific complex mechanisms occur at each scale (macro-scale = 10^{-2}-10^{3}m, meso-scale = 10^{-3}-1m, micro-scale 10^{-6}-10^{-2}m), the use of idealized propagation models often limits the analysis to a single scale of investigation and oversimplifies the prediction of stress and deformation. In most numerical schemes, the presence of micro-cracks in the bulk of the rock mass is accounted for indirectly: either by modeling a plastic zone (Liu 1984; Hamiel et al. 2004a; Busetti et al. 2012; Shen 2012; Smart et al. 2012), or by defining a "process-zone stress" (Ramurthy et al. 2009a; Ramurthy et al. 2009b) that is used to calculate the stress intensity factor in the surrounding of fractures. Most fracture propagation models neglect the presence of micro-scale discontinuities in the process zone (Shlyapobersky and Chudnovsky 1994). Neglecting the effects of micro-cracks leads to ignoring the degradation of solid stiffness, and therefore, to underestimating fracture toughness and over estimating fracture propagation, which, for example, could lead to errors in determining hydraulic fracture initiation pressure (Ramurthy et al. 2009a). Recent studies established an explicit relationship between rock grain size distribution and the dimensions of the fracture process zone (Tarokh and Fakhimi 2013), which illustrates the importance of relating rock fabric to rock stiffness in the surrounding of large-scale discontinuities. Oda (1984) and Lubarda and Krajcinovic (1993) related micro-crack density and orientations to a mesoscopic fabric tensor. Cowin (1985) related the fabric tensor to the elastic stiffness tensor without resorting to any sort of homogenization scheme. Economides and Valko (1994), Valko and Economides

(1993, 1994) postulated the expression of a modified fracture toughness to predict fracture propagation in a damaged rock mass. The macroscopic fracture reaches a given location when the mesoscopic damage variable at that location is equal to unity. Wu and Chudnovsky (1993) studied the influence of a static array of micro-cracks on fracture propagation. The framework assumes that the micro-cracks do not propagate. Therefore, the interaction between fracture propagation and damage evolution is not captured in the model. Suzuki (2012) modeled the interactions between micro-crack nucleation and kinking and the growth of a shear fault plane. However, the defects (at both the microscopic and macroscopic scales) are all considered to be flat debonded surfaces. Therefore the model cannot be extended to fracturing problems with fluid injection, in which fracture aperture and crack-induced porosity play an important role in the viscosity fracture propagation regime. Purely mechanistic models were recently proposed to explain the interaction between stress reorientation and rock stiffness softening around dynamic shear faults (Yamashita 2000; Faulkner et al. 2006; Healy 2008; Heap et al. 2010). These studies focus on flat micro-crack nucleation, flat fracture tip propagation, and plane fault slip. Capturing the transition from fracture nucleation, which occurs at the microscale, to propagation and interaction at the meso-and macro-scales, is a challenge in modeling fracturing processes due to complications including simulating growth as a function of time, coupling equations, and time-stepping (Adachi et al. 2007). The numerical solution is highly mesh-dependent: the localized zone narrows with mesh-refinement, and non-structured meshes lead to a non-symmetric plastic zone even when the problem is symmetric relatively to the fracture plane.

The goal of this study is to capture the effects of micro-crack induced damage in shale, by using the Finite Element Method (FEM). The approach is based on the implementation of a robust material model that can be used in both continuous and discontinuous media. CDM provides a suitable theoretical framework to relate geometrical fabric tensors (with various types of micro-cracks in different directions) to stiffness, and therefore, predict the degradation of rock mechanical properties subsequent to damage propagation (Lyakhovsky et al. 1997; Hamiel et al. 2004b; Colovos et al. 2013; Gaede et al. 2013). Combining finite element modeling to a CDM-based constitu-

tive model of damage allows simulating a range of realistic geometric configurations at different scales, in three dimensions. For example in reservoir production models anisotropic damage can be linked to permeability enhancement within the quasi-elastic domain to improve reservoir forecasting models (Shalev and Lyakhovsky 2013; Xu and Prévost 2016). Anisotropic damage was also used in tectonic deformation models as a proxy for heterogeneous natural fracturing (Busetti et al. 2014). Implementation of peak strength and post-failure softening and coupling with macro-crack propagation are outside of the current scope but will be addressed in future enhancements to the model.

Section 2 presents the theoretical outline, the calibration and the verification of the Differential Stress Induced Damage model (DSID) (Xu and Arson 2014) used herein to predict the stress-strain response of shale. The DSID model was implemented using the FEM in MATLAB (a multi-paradigm numerical computing environment and fourth-generation programming language developed by MathWorks (Matlab)) and ABAQUS (a product of Simulia, a division of Dassault Systèmes (Abaqus)). The model allows predicting the initiation and propagation of cracks in the damaged zone surrounding large-scale discontinuities such as faults or hydraulic fractures. A second-order-tensor damage variable is used to indirectly couple the micro- and meso- scales, similar to the fabric tensor introduced by Oda (Oda 1984; Cowin 1985). The damage variable gives a representation of distributions of micro-cracks several orders of magnitude smaller than the large-scale discontinuity. Triaxial compression tests from *ConocoPhillips*' subsurface core from the Bakken shale, Williston Basin, North Dakota, were used to calibrate a representative DSID model. Details on the experiments are provided in (Amendt et al. 2013). Calibrations were conducted for a representative sample set from the Bakken formation. Experimental stress-strain curves from a few representative rock mechanics tests in the Middle Bakken member, a low porosity ($< 10\%$) tight calcareous mudstone, were used to compare the difference between experimental and numerical results. In Section 3, a Finite Element analysis is presented, to study the effects of sample size on stress concentrations and damage localization, and predict the anisotropy induced by microscopic crack propagation in initially isotropic and anisotropic shale samples. Triaxial compression tests

were simulated using both the standard ASTM 25.4×50.8 mm cylindrical plug dimensions used in the laboratory tests, as well as larger 101.6×152.4 mm whole core size. The distribution of stress around a bedding delamination plane was computed with a smeared damaged zone model, and compared to that obtained with a discrete fracture model.

OUTLINE OF THE DSID MODEL: A DAMAGE MODEL FOR FRACTURES PROCESS ZONE

Continuum methods usually predict the behavior of the material with phenomenological approaches at meso-scale. For example, the disturbed state concept (DSC) presented in (Desai 2000; Desai 2015) is a model in which the fully adjusted (degraded or strengthened) material remains a continuum with updated properties. The model can relate the initiation and growth of microcracking with its state variables to macroscopic status, such as stresses and deformations. An internal length parameter is implicitly accounted for (Desai et al. 1997) in the DSC. However, the state variables in the DSC cannot indicate the evolution of the characteristic features (geometry, arrangement or orientation) of the microcracks, which leads the non-local nature of the DSC is limited. It needs to be enriched with micro-mechanics to capture the evolution of these characteristic features. The Differential Stress Induced Damage (DSID) is proposed to couple the damaged and undamaged part of a continuum but are limited to the coupling between micro-scale crack propagation and meso-scale damage propagation. The equations of the damage model previously formulated by two of the authors (Xu and Arson 2014) decompose the total strains into pure elastic part, irreversible part (due to crack opening), and elasto-damage part (the coupling between elastic part and damaged part). The model expression contains the internal length of the microcracks implicitly as well (Jin et al. 2016). Besides that, the DSID can provide with assumptions on microcracks' geometry and orientation based on the model's hypothesis. The details of the DSID model are summarized in the following sections.

Definition of the REV and meaning of the damage variable

The DSID model allows predicting mechanical anisotropy induced by a reorientation of stress principal directions in the rock mass (change of differential stress) and associated damage weak-

ening. The damage variable $\boldsymbol{\Omega}$ is the crack density tensor defined by Kachanov (1992), projected in its principal base:

$$\boldsymbol{\Omega} = \sum_{k=1}^{3} \rho_k \boldsymbol{n_k} \otimes \boldsymbol{n_k} \tag{1}$$

The k-th eigenvalue of damage (ρ_k) is the porosity of all the crack planes oriented perpendicular to the k-th direction of space ($\boldsymbol{n_k}$). For instance the vertical damage Ω_{11} represents the volume fraction of penny shaped cracks parallel to a plane of normal $\boldsymbol{n_1}$, i.e. the volume fraction of horizontal cracks. Similarly, horizontal (or lateral) damage components Ω_{22} and Ω_{33} represent the volume fractions of penny-shaped cracks parallel to planes of normal $\boldsymbol{n_2}$ and $\boldsymbol{n_3}$ respectively, i.e. the volume fraction of vertical cracks. Damage is a symmetric second rank tensor which characterizes the arrangement of the microstructural components in a multiphase or porous material (Cowin 1985). As illustrated in Figure 1, the damage variable is similar to Oda's fabric tensor (Oda 1984), and is used to predict damage-induced anisotropy of deformation and stiffness.

The DSID model is formulated at the mesoscale in order to predict damaged elastic properties that can be measured in the laboratory on a Representative Elementary Volume (REV - $10^{-3}\,m$ - $1\,m$). Damage is equivalent to three mesocracks at the REV scale: each mesocrack is oriented perpendicular to one of the three damage eigenvectors, with a volume fraction equal to the porosity of all the micro-cracks oriented in that same direction. This representation assumes that micro-cracks that have approximately the same normal vector can be gathered into families of micro-cracks of same orientation (Arson 2009). The REV should be at least two orders of magnitude larger than the typical size of a micro-crack (Horii and Nemat-Nasser 1986). The REV can either be defined to represent the average behavior of a family of parallel micro-cracks (Figure 2. a) or the evolution of one micro-crack that does not interact with the other micro-cracks located in its surroundings (Figure 2. b).

In the DSID model, the evolution law of the damage tensor is chosen so as to capture the expected evolution of rock stiffness upon micro-crack propagation. Figure 3 explains how the propagation of the REV-scale mesocrack affects the stiffness tensor, in the hypothetical case of unidirectional damage. The DSID model captures damage propagation and damage initiation.

Therefore, in the reference state, it is assumed that the REV contains an initial crack of length l_0, which means that the initial stiffness is less than the undamaged stiffness of a homogeneous solid: this is represented by a broken spring in Figure 3.a. The length of the crack remains the same as long as the material is in the elastic domain. After the crack propagation threshold is reached, the mesocrack propagates and becomes longer ($l > l_0$), and stiffness in the direction orthogonal to the mesocrack decreases. This is represented by an increased number of broken springs in Figure 3.b.

Multiple mechanisms (including crack propagation in tension and compression for instance) are most often modeled by coupling damage and plastic potentials (Cicekli et al. 2007), which tremendously increases the model complexity and the number of material parameters involved. To facilitate numerical implementation and convergence, the DSID model accounts for material non-linearity using a modified hyper-elastic framework, where a single energy dissipation function is used to predict damage evolution and irreversible crack-induced deformation. The total deformation tensor ($\boldsymbol{\epsilon}$) is split as follows:

$$\boldsymbol{\epsilon} = \boldsymbol{\epsilon}^{\boldsymbol{E}} + \boldsymbol{\epsilon}^{\boldsymbol{id}} = \boldsymbol{\epsilon}^{\boldsymbol{el}} + \boldsymbol{\epsilon}^{\boldsymbol{ed}} + \boldsymbol{\epsilon}^{\boldsymbol{id}} \tag{2}$$

in which $\boldsymbol{\epsilon}^{\boldsymbol{el}}$ is the purely elastic deformation (undamaged part), which would be produced in the absence of damage); $\boldsymbol{\epsilon}^{\boldsymbol{ed}}$ is the additional recoverable deformation that results from stiffness degradation (coupled terms accounting for both damaged and damaged parts); $\boldsymbol{\epsilon}^{\boldsymbol{id}}$ is the irreversible crack-induced deformation, which represents the existence of residual crack openings after unloading (damaged part). Although the DSID model assumes no residual strength in the damaged part, mechanical interactions between the undamaged and damaged parts are accounted for through the elasto-damage term $\boldsymbol{\epsilon}^{\boldsymbol{ed}}$, in the sense that damage results from both elastic and crack-induced irreversible deformation. $\boldsymbol{\epsilon}^{\boldsymbol{E}} = \boldsymbol{\epsilon}^{\boldsymbol{el}} + \boldsymbol{\epsilon}^{\boldsymbol{ed}}$ is the total recoverable deformation. In the proposed model, emphasis is put on solving for the full damage tensor in order to capture the evolution of anisotropic microcrack generation under applied loading (differential stress). The thermodynamic framework of the DSID model is explained in the following subsections. In summary, damage evolution is

controlled by a damage function, similar to Drucker-Prager yield function (but depending on the energy release rate due to damage, instead of stress). The damage flow rule is non-associated, and the damage potential is chosen to ensure the positivity of the damage dissipation potential. The flow rule of the irreversible deformation is associated, and avoids the irreversible strain development contradicting the damage evolution induced by deviatoric stress.

Thermodynamic framework of the DSID model

The free energy stored in the REV considered is transformed into deformation energy and heat, or dissipated in the form of irreversible microstructure changes (e.g. damage and irreversible deformation). Deformation and dissipation variables are work-conjugate to stress and force variables, and can be obtained by deriving the free energy potential.

Free energy

The expression of the free energy considered in the DSID model is a polynomial of order two in stress, and of order one in damage (Shao et al. 2005):

$$\begin{aligned} G_s(\boldsymbol{\sigma}, \boldsymbol{\Omega}) = \frac{1}{2}\boldsymbol{\sigma} : \mathbb{S}_0 : \boldsymbol{\sigma} + a_1\,\mathrm{Tr}\boldsymbol{\Omega}(\mathrm{Tr}\boldsymbol{\sigma})^2 + a_2\,\mathrm{Tr}(\boldsymbol{\sigma}\cdot\boldsymbol{\sigma}\cdot\boldsymbol{\Omega}) \\ + a_3 \mathrm{Tr}\boldsymbol{\sigma}\mathrm{Tr}(\boldsymbol{\Omega}\cdot\boldsymbol{\sigma}) + a_4 \mathrm{Tr}\boldsymbol{\Omega}\mathrm{Tr}(\boldsymbol{\sigma}\cdot\boldsymbol{\sigma}) \end{aligned} \tag{3}$$

Where G_s is the Gibbs free energy; $\boldsymbol{\sigma}$ is the stress; $\boldsymbol{\Omega}$ is the damage variable; $\mathbb{S}_0$ is the initial compliance tensor; and a_i are material parameters. The total elastic strain $\boldsymbol{\varepsilon}^E$ (ratio between the total elastic displacement and original material length) is conjugated to stress (which can be computed from the external load). Conjugation relationships write:

$$\begin{aligned} \boldsymbol{\varepsilon}^E = \frac{\partial G_s}{\partial \boldsymbol{\sigma}} = \frac{1+\nu_0}{E_0}\boldsymbol{\sigma} - \frac{\nu_0}{E_0}(\mathrm{Tr}\boldsymbol{\sigma})\,\boldsymbol{\delta} + 2a_1(\mathrm{Tr}\boldsymbol{\Omega}\,\mathrm{Tr}\boldsymbol{\sigma})\,\boldsymbol{\sigma} + a_2(\boldsymbol{\sigma}\cdot\boldsymbol{\Omega} + \boldsymbol{\Omega}\cdot\boldsymbol{\sigma}) \\ + a_3[\,\mathrm{Tr}(\boldsymbol{\sigma}\cdot\boldsymbol{\Omega})\,\boldsymbol{\delta} + (\mathrm{Tr}\boldsymbol{\sigma})\,\boldsymbol{\Omega}\,] + 2a_4(\mathrm{Tr}\boldsymbol{\Omega})\,\boldsymbol{\sigma} \end{aligned} \tag{4}$$

Where ν_0 and E_0 are the initial Poisson's ratio and Young's modulus. The damage variable is used to describe the degradation of the stiffness upon crack propagation. The damage driving force $\mathbf{Y}$

is defined as the partial derivative of the free energy by damage:

$$\mathbf{Y} = \frac{\partial G_s}{\partial \mathbf{\Omega}} = a_1(\mathrm{Tr}\boldsymbol{\sigma})^2\,\boldsymbol{\delta} + a_2\boldsymbol{\sigma}\cdot\boldsymbol{\sigma} + a_3\mathrm{Tr}(\boldsymbol{\sigma})\boldsymbol{\sigma} + a_4\mathrm{Tr}(\boldsymbol{\sigma}\cdot\boldsymbol{\sigma})\boldsymbol{\delta} \tag{5}$$

Where $\boldsymbol{\delta}$ is the second-order identity tensor (Kronecker delta)

Damage function

CDM initially aimed to model brittle behavior observed in metals (Krajcinovic 1996; Lemaître and Desmorat 2005). In early damage models proposed for concrete (Mazars 1986; Mazars and Pijaudier-Cabot 1989), two damage scalar variables were introduced in order to distinguish stiffness degradation rates in tension and compression. Following the same idea, Frémond (Frémond and Nedjar 1996) split the damaged elastic deformation energy into potentials associated to tension and compression. Damage evolution laws are made dependent on negative and positive strains, for compression and tension, respectively. The formulation allows modeling unilateral effects of crack closure on stiffness, i.e. the recovery of compression strength without recovery of tension strength when cracks close. Note that damage models resorting to two different scalar variables are weakly anisotropic models: the determination of the principal directions of the strain (or stress) tensor is necessary to evaluate the energy dissipated in tension and in compression. However the scalar form adopted for the damage variables does not allow predicting damage-induced anisotropy: anisotropy of strain (or stress) controls damage rates, but stiffness anisotropy does not depend on damage. In Lubliner's concrete damage model (Lubliner et al. 1989), the damage variable is defined as the ratio of dissipated plastic energy for both tensile and compressive cases. Based on this framework, (Lee and Fenves 1998) coupled damage and plasticity by using different hardening variables for different stress states. Damage models that are not coupled to plasticity require the definition of damage potentials. (Abu Al-Rub and Kim 2010) used two separate potentials for two different damage variables (damage due to tensile stress, damage due to compressive stress). In Frémond's model (Frémond and Nedjar 1996), the variables that are work-conjugate to damage variables (called "affinities" or "energy release rates") are discontinuous functions of strain: $\partial\Psi_s/\partial\beta_c$ de-

pends on ε^-, and $\partial\Psi_s/\partial\beta_t$ depends on ε^+. This implies that the rate of damage depends on a non-differentiable field function. The rate of damage (computed from the normality rule) is not unique at singularity points, which raises important numerical issues.

In geomaterials such as rock and concrete, compression strength typically differs by one order of magnitude from tensile strength. Although damage under isotropic compression was observed in hardened cement paste (Ghabezloo et al. 2008), "compression damage" in geomaterials is in general associated to cracking under a differential stress. Let us consider a brittle material sample subjected to a triaxial compression stress. If the sample is homogeneous and if there is no friction at the top and bottom boundaries, the sample undergoes lateral expansion. If boundaries are frictional and the sample is homogeneous, shear cracks will form. The granular fabric of rock and concrete tends to drive cracks around the stiffest crystals or aggregates, which results in "splitting effects" in tension and "crossing effects" in compression (Ortiz 1985). In CDM, crossing effects in geomaterials are modeled as tension damage: a crack parallel to the axis, driven by axial compression, is considered to have the same mechanical effects as a crack parallel to the axis, driven by lateral tension. Based on the concepts of splitting and crossing effects, we define the following damage function f_d to control the triggering of anisotropic damage in the DSID model:

$$f_d\left(\mathbf{Y},\mathbf{\Omega}\right) = \sqrt{J^*} - \alpha I^* - k \tag{6}$$

In which:

$$J^* = \frac{1}{2}(\mathbb{P}_1 : \mathbf{Y} - \frac{1}{3}I^*\boldsymbol{\delta}) : (\mathbb{P}_1 : \mathbf{Y} - \frac{1}{3}I^*\boldsymbol{\delta}), \quad I^* = (\mathbb{P}_1 : \mathbf{Y}) : \boldsymbol{\delta} \tag{7}$$

The projection tensor $\mathbb{P}_1$ is introduced in order to constrain the damage driving force to remain parallel to the external stress load:

$$\mathbb{P}_1\left(\boldsymbol{\sigma}\right) = \sum_{p=1}^{3}\left[H(\sigma^{(p)}) - H(-\sigma^{(p)})\right]\mathbf{n}^{(p)}\otimes\mathbf{n}^{(p)}\otimes\mathbf{n}^{(p)}\otimes\mathbf{n}^{(p)} \tag{8}$$

Where $H(\cdot)$ is the Heaviside function. The damage threshold k is the sum of an initial damage threshold (C_0) and an additional term that accounts for damage hardening effects (controlled by the parameter C_1):

$$k = C_0 + C_1 \mathrm{Tr}\left(\mathbf{\Omega}\right) \tag{9}$$

Damage potential

A non-associated damage flow rule is employed: the direction and magnitude of the damage increment are obtained by deriving the following damage potential (g_d):

$$g_d = \sqrt{\frac{1}{2}(\mathbb{P}_2 : \mathbf{Y}) : (\mathbb{P}_2 : \mathbf{Y})} - C_2 \tag{10}$$

The projection tensor $\mathbb{P}_2$ ensures that damage propagates in the direction parallel to the deviatoric stress (the projector ensures that only tensile deviatoric stress can trigger damage):

$$\mathbb{P}_2 = \sum_{p=1}^{3} H\left[\max_{q=1}^{3}(\sigma^{(q)}) - \sigma^{(p)}\right] \mathbf{n}^{(p)} \otimes \mathbf{n}^{(p)} \otimes \mathbf{n}^{(p)} \otimes \mathbf{n}^{(p)} \tag{11}$$

Note that according to equations 6-11, damage propagates as long as the net difference between two principal stresses exceeds a certain value. Thus the DSID model can handle both compression and tension-driven crack propagation. The DISD model assumes that the critical energy release rate necessary to trigger damage is the same in all directions of space, and for both compressive and tensile behaviors (note that different thresholds could be used to distinguish tensile and compressive rock strength).

Flow rules

Flow rules are used to calculate the damage increment and the irreversible strain increment. An associated flow rule is used for the irreversible strain rate $\dot{\boldsymbol{\varepsilon}}^{id}$ (which means that the damage potential is assumed to be equal to the damage function); whereas a non-associated flow rule is

used for the damage rate, $\dot{\mathbf{\Omega}}$ (from the damage potential, which is different from damage function):

$$\dot{\boldsymbol{\varepsilon}}^{id} = \dot{\lambda}_d \frac{\partial f_d}{\partial \boldsymbol{\sigma}} = \dot{\lambda}_d \frac{\partial f_d}{\partial \mathbf{Y}} \frac{\partial \mathbf{Y}}{\partial \boldsymbol{\sigma}} \tag{12}$$

$$\dot{\mathbf{\Omega}} = \dot{\lambda} \frac{\partial g_d}{\partial \mathbf{Y}} \tag{13}$$

Where $\dot{\lambda}_d$ is the Lagrangian Multiplier which is the magnitude of the irreversible strain here.

Principle of the DSID model for shale brittle deformation regime

Shale is the generic name used for any fine grained sedimentary rock characterized by discontinuities along thin laminae or parallel layering or bedding (Figure 4a). Shales can include a range of distinct low porosity and permeability lithologies (e.g., marl, mudstone) with varying amounts of silica, carbonate, clay, and organic content (kerogen). Samples used to characterize shale mechanical properties are cut from the full coring diameter (commonly 63.5 mm -133.4 mm diameter whole core), in order to get long plugs, 25.4 mm diameter by 50.8 mm long. Often, plugs are cored parallel and perpendicular to the bedding planes, in order to obtain homogeneous test samples more easily, and to determine mechanical properties in the principal fabric directions of the rock, controlled by fine depositional layering or bedding due to delamination ("poker chipping"). To calibrate the DSID model, a set of laboratory triaxial compression tests from the Middle Bakken member of Bakken shale were used (see details in (Amendt et al. 2013)). The Middle Bakken samples used in this study were composed mostly of carbonate (45%), silica (30%), clay (>10%), void space (porosity <10%), kerogen and other (<10%), heterogeneously distributed in fine laminations (Figure 4a). Although the optimal plugs for triaxial testing contain no flaws, in some rock intervals the presence of microcracks, and bedding planes, some of which were being fully delaminated, is unavoidable (Amendt et al. 2013).

A typical stress-strain path for rock under triaxial compression test is shown in Figure 5. Three main deformation regimes are noted. First, shale exhibits a quasi-linear elastic behavior. Zone I describes the linear elastic behavior of the rock (characterized by Young's modulus and Poisson's ratio), defined by fully reversible deformation and no hysteresis. It is important to note that zone I

may also include the early onset of strain hardening: elastic moduli measured upon unloading are lower than the ones of the pristine rock, due to microcrack generation. The true elastic response of shale has been observed to be a small portion of the curve represented in zone I. Zone II exhibits the onset of ductile behavior: plastic deformation accumulates with increased axial loading. Irreversible strains are more dominant than during the quasi-linear elastic deformation regime in zone I. Zone III is the post-peak domain, which starts at the failure point. After failure, the sample is fully fractured and stress drops to the residual strength of the rock. In zone III, microcracks rapidly intersect and coalesce to form a propagating macroscopic fracture, therefore the strength of the rock also decreases rapidly. The present work focuses on zone I, i.e. the quasi-linear elastic regime, which is assumed to consist primarily of reversible deformation followed by the onset of early brittle microcracking. It is within this deformation stage in shale, prior to significant plastic yielding, that pervasive microcracking, stiffness and strength reduction, and heterogeneous material degradation occur within heterogeneously stressed portions of the rock (e.g., areas of local stress amplification). Classical linear elastic models cannot capture this early strain hardening phenomenon. Non-linear elastic models could capture strain hardening, but not the decrease of elastic moduli resulting from crack propagation. The DSID model allows predicting both damage heterogeneity and anisotropic stiffness degradation induced by deformation and microcrack propagation, as described by the associated energy dissipation.

Calibration of DSID model parameters

Triaxial compression tests provided by *ConocoPhillips* were used to determine the DSID model parameters. The calibration was done iteratively with a dedicated MATLAB code. The algorithm was similar to the one used in the Maximum Likelihood Method presented in (Bakhtiary et al. 2014), except that the optimization problem was solved by minimizing the squared residuals of the distance, r_i, between experimental data, y_i, and numerical predictions, $f(\mathbf{x}, \mathbf{B})$:

$$S = \sum_{i=1}^{n} r_i^2, \qquad r_i = y_i - f(\mathbf{x}, \mathbf{B}) \tag{14}$$

Where $\mathbf{x}$ stands for the vector of known input variables and $\mathbf{B}$ is the vector of parameters that need to be calibrated. The algorithm was initialized with the mean, minimum and maximum values of the model parameters. Using these parameters, a triaxial compression test was simulated at the material point using the DSID model. The gradient method was employed to minimize the difference between numerical and experimental stress-strain curves, and find the optimal set of parameters. The algorithm started with the initialized vector $\mathbf{B}_0$, and iteratively finds the sequence $\mathbf{B}_1, \mathbf{B}_2, \ldots \mathbf{B}_{n+1}$ by solving:

$$\mathbf{B}_{n+1} = \mathbf{B}_n - \gamma_n \nabla f(\mathbf{B}_n) \tag{15}$$

In which the value of the step size γ_n is allowed to change at each iteration.

The stress-strain curve used for model calibration was obtained for a rock sample taken from the subsurface core that was first subjected to a 4,000 psi (27.6 MPa) isotropic compressive stress, and then subjected to a contractional axial strain (which causes some deviatoric stress in the sample). The Young's modulus and Poisson's ratio in the reference state were read from the experimental stress-strain curve, and the remainder of the DSID parameters were calibrated iteratively. Results are reported in Table 1. Figure 6 shows the experimental stress-strain curve (in blue) and the numerical stress-strain curve obtained after model calibration (in red). At a given axial (respectively lateral) strain, the maximum difference between the value of the deviatoric stress measured in the experiments and that calculated with the DSID model is less than 13% (respectively 9%), which is on the same order as the measured variability between samples taken from the same depth, where minor differences in the experimental data are due to intrinsic lithologic heterogeneity. Although it is possible to fine-tune the calibration for each triaxial plug, the calibrated stress-strain curve instead reflects representative behavior for the particular Bakken shale depth interval. Therefore we consider that both axial and radial strains predicted with the DSID model match experimental results within acceptable limits. A parametric study was conducted in order to assess the sensitivity of the model to the hardening parameter C_1: the range of variations of the stress-strain curves is shaded in gray in Figure 6. This sensitivity analysis shows that deformation and damage increase when C_1 decreases.

In the calibration proposed above, the damage threshold was assumed to be reached at less than 0.005% axial strain, and the reference elastic moduli were computed from the slopes of the lines joining the origin of the stress-strain plot to the points where damage first occurred in the axial and radial directions. The value considered for E_0 was higher than the values reported by the lab for the particular Bakken shale samples. This is because the definition of a reference mechanical state is by itself contingent upon the level of accuracy with which damage triggering is detected during the triaxial compression test. Within the CDM framework adopted herein, rock is viewed as a damaged material, even in the initial state. If a change of slope in the stress-strain curve is detected in the early stage of the brittle deformation regime (zone I in Figure 5), the damage threshold will be low, and the corresponding reference stiffness will be high. The estimation of the reference elastic properties E_0 and ν_0 is a long-standing research issue. In previous modeling publications (Halm and Dragon 2002; Hayakawa and Murakami 1997), authors proposed calibration methods in which the damage threshold (C_0) was estimated manually, from the modeler's judgment. Some experimental works considered the onset of damage to occur at the point where the volumetric strain curve inverts (Crawford and Wylie 1987; Pagoulatos 2004), which may correspond to an increase in acoustic emission activity (Paterson 1978; Butt and Calder 1998) associated with microcracking. Other studies (Katz and Reches 2004) used microscopic mapping techniques to link damage onset with a change in the derivative of the axial strain curve, reflecting reduced elastic stiffness. The second author (S. Busetti) previously applied both the volumetric and axial strain methods to the Bakken shale data set and found the actual damage initiation point to be ambiguous compared to the sandstone and granite samples of the prior publications. Additional experimental study using acoustic emissions or microcrack mapping would be required to better constrain the damage threshold in these samples. Three different damage thresholds were estimated from the experimental stress-strain curve of a triaxial compression test performed under 3,000 psi (20.7 MPa) confining stress. The corresponding values found for the reference Young's modulus and Poisson's ratio are reported in Table 2. For the three different thresholds estimated, the calibrated damage parameters were used to simulate the triaxial compression test conducted under 3,000 psi

(20.7 MPa) confining stress. The comparison between the experimental and numerical stress-strain plots, shown in Figure 7, indicates that a better accuracy is achieved for higher reference Young's modulus. This was expected, because a high reference Young's modulus was considered in the calibration of the DSID model under 4,000 psi (27.6 MPa) confining stress. The differences noted between the plots obtained with different sets of reference elastic moduli also highlight the dependence of rock mechanical stiffness to confining pressure, which is accounted for in the DSID model as soon as the rock REV is in the damage domain: damage propagates faster under higher differential stress.

The calibrated DSID model was verified against stress-strain curves obtained during triaxial compression tests conducted under 1,000 psi (6.9 MPa); 2,000 psi (13.8 MPa); and 3,000 psi (20.7 MPa) confining stress. For each verification test, the Young's modulus and Poisson's ratio were calculated from the experimental stress-strain plots, by choosing the damage threshold manually (Table 3). The comparison between experimental and numerical responses is shown in Figure 8. As expected, higher the confining stress, higher the reference Young's modulus (because confining stress tends to close initial defects and stiffen the rock).

FINITE ELEMENT SIMULATION OF LABORATORY TESTS

A UMAT subroutine was written in order to use the DSID model in ABAQUS Finite Element software. Triaxial compression tests were simulated at the scale of the whole core and at the scale of a standard plug sample, in two stages: first, an isotropic confining stress of 4,000 psi (27.6 MPa) was applied on the top, bottom and lateral boundaries of the domain; second, the top and bottom boundaries were subjected to an axial displacement of equal magnitude (given in the following sections), under constant lateral confining stress. The simulations presented below aim to study the effects of sample size, intrinsic anisotropy and initial delamination planes on the overall mechanical response of shale under states of differential stress. All the simulations were conducted with the optimum set of parameters reported in Table 1, with hexahedral linear elements (each element had 8 integration points). Both the rock specimen and the metal platens at the top and bottom of the sample were modeled with the FEM. At the interface between the rock sample

and the metal platens, normal and tangential displacements were constrained by a normal non-penetration condition and a friction law (Figure 9). Before the critical shear stress limit line is reached, the surfaces are fully bonded. If the equivalent shear stress exceeds the critical line, the surfaces start to slide. The equivalent shear stress is computed as:

$$\overline{\tau} = \sqrt{\sum_{i=1}^{n} \tau_i^2} \tag{16}$$

For the rock/metal contact, a friction coefficient $\mu = 0.8$ was adopted.

Effect of sample size on stress concentrations and damage localization

The finite element model simulates a plug deformed under triaxial compression loading conditions (Figure 10). The laboratory experiments were conducted on 50.8 mm long by 25.4 mm diameter plugs cut from subsurface core of the Bakken Shale. The sample is loaded in a triaxial cell by first applying confining pressure to the sides of the sample via a jacket until the overall confinement level is reached (4,000 psi, i.e. 27.6 MPa, in the case studied here). Next, axial displacement is applied vertically at a strain rate of $10^{-5}\, s^{-1}$ applied by moving pistons that act on the sample by metal platens, which are in frictional contact with the rock plug. Axial displacement at the pistons and radial displacement using strain gauges attached to the sample recorded incremental deformation. The laboratory sample was then loaded through failure and post-failure to capture the full deformation cycle. The finite element model reflects a simplified version of the laboratory experiment and allows for direct comparison of the constitutive behavior at the element level in different regions of deformation (e.g., center versus edges of the plug) with the overall constitutive behavior as derived from the laboratory sampling approach. Two Finite Element models were compared:

- The standard size recommended by the American Society for Testing and Materials (ASTM) for plug tests: 1 inch (25.4 mm) in diameter and 2 inch (50.8 mm) in height;
- A portion of whole core: 101.4 mm in diameter and 152.4 mm in height.

We ran a range of tests changing the mesh size from 0.8 mm to 5 mm. Element sizes ranging from 0.8 mm to 5 mm showed minimal variation on the deformation pattern and were accurate within 3%. The element size of 2.5mm giving a 1% error was therefore considered appropriate to capture strain heterogeneity and the onset of damage localization. In order to focus the comparison on sample size effects, both the plug test and the core test were simulated with Finite Elements of the same size: $2.5 \times 2.5 \times 2.5$ mm. 2,200 elements were used to model the plug, and 93,208 elements were used to model the whole core.

Figures 11-12 show the vertical stress σ_{11} concentration at the edges of the contact surfaces between the platens and the rock specimen. Stress decreases gradually from the edges to the center of the contact surface. Boundary effects decrease from the platens to the center of the sample. For the two sample sizes tested, the vertical stress distribution is not uniform. Stress in elements located in the middle of the sample is not equal to the stress applied at the boundary. Stress components in the other directions (not shown here) also exhibit a heterogeneous (i.e., non uniform) and anisotropic (i.e. directionally variant) distribution in the sample. At certain loadsteps, the lateral confining pressure exceeds the vertical compression, which induces vertical damage (i.e., horizontal cracks). By contrast, horizontal damage represents vertical micro-cracks that open because the vertical compression stress exceeds the lateral confining stress, and concentrates in the corners of the sample (Figure 13). As expected, vertical damage is minimal during the triaxial compression test (Figure 14).

In order to assess the boundary effects noted above, the stress-strain curve computed in a central element of the mesh was compared to the stress-strain curve obtained numerically with the MATLAB code written to simulate one-element tests. The one-element test corresponds to ideal conditions - with no edge effects. Figure 15 shows the axial loading phase of the triaxial compression test, for the one-element simulation and for the two Finite Element models described in Figure 10. Note that for consistency, the strains at the end of the confining stage were subtracted from the cumulated strains, which explains why the plots start at zero strains in Figure 15. As expected, simulation results obtained with the FEM show some deviation from the ideal stress-

strain curve predicted in the one-element simulation (figure 16). The error of the stress deviation from the one-element test for both FEM simulations are checked at the same strain levels. Overall, results are more sensitive to lateral strains. Despite stress heterogeneity in the sample due to edge effects ($<$10% variability for both tests in axial strains, and $>$10% in lateral strains) stress-strain curves obtained in individual Finite Elements are similar to the ones obtained at the material point with MATLAB. Higher heterogeneity and stress concentration was noted in the whole core sample, because simulations involved the same element size but a larger domain than in the plug test. Consequently, higher departure from the reference one-element test is noted in the results obtained for the whole core sample test than for the plug test, especially for the radial strains. The pattern of stress observed within the whole core sample is a main departure from uniformity assumption required for property calibrations, and should be considered when calibrating to lab and field tests. Overall, edge effects do not appear to significantly affect the overall constitutive response of elements in the model, and the finite element simulations are considered acceptable at both scales. These findings suggest that for the quasi-linear elastic deformation stage (zone I, Figure 5), the single-element calibrated material model is suitably scalable to larger geometric configurations in order to predict stress concentrations and damage localization.

Effect of initial anisotropy on stress-induced anisotropy

Due to sedimentary deposition, shale is naturally anisotropic. The DSID model can be used to account for initial anisotropy (existing prior to loading), and for stress-induced anisotropy (due to damage propagation in the three directions of space). Note that in the following, $\Omega = 0$ refers to intact rock and $\Omega = 1$ refers to a state of pervasive microcracking. The current version of the DSID model is limited to pervasive microcracking with no crack coalescence (zone I in Figure 5); therefore, the DSID model cannot be used to predict full weakening (zero strength). The triaxial compression test described above was simulated for a plug 25.4 mm in diameter, and 50.8 mm in height, for the following initial damage conditions:

- No initial damage: the sample is initially homogeneous and isotropic ($\Omega_{11} = \Omega_{22} = \Omega_{33} =$

0), where direction 1 is vertical and directions 2 and 3 are in the horizontal plane;

- Initial damage in the lateral directions ($\Omega_{11} = 0$, $\Omega_{22} = \Omega_{33} = 0.1$), this condition represents natural microcracking damage (vertical cracks), due to tectonic loading, or uplift for instance;
- Initial damage in the vertical direction ($\Omega_{11} = 0.1$, $\Omega_{22} = \Omega_{33} = 0$), this condition represents bedding delamination planes (horizontal cracks).

In the second loading phase, a vertical strain of 0.8% was applied. The ratio between the vertical elastic modulus and horizontal elastic modulus is used as an anisotropy index:

$$\alpha = \frac{E_1}{E_3} \tag{17}$$

Figure 17 illustrates the evolution of stiffness anisotropy for an element with no initial damage, i.e., initially isotropic. Isotropic materials have an elastic anisotropy index of $\alpha = 1$ at the beginning of the axial loading stage. Damage propagates as differential stress increases, which results in a decrease of the elastic moduli. However, vertical microcracks are more prone to open during the axial loading, so that the horizontal Young's moduli E_2 and E_3 decrease faster than the vertical modulus E_1.

Figure 18 shows the changes of Young's modulus observed during the tests, normalized by the initial undamaged modulus. Note that the modulus plotted was the one calculated in a central element of the mesh, in which the axial strain is not equal to the loading strain. This explains why the final axial strain is not the same for the samples tested. This difference does not change the conclusions drawn from the results concerning the evolution of mechanical anisotropy. During the initial confinement loading stage, damage weakening occurs. The pre-damaged samples (red and green lines, Figure 18) experience less stiffness reduction than the samples without pre-damage (blue lines, Figure 18)). In other words, the existence of pre-existing micro-cracks in the sample makes the material more compliant, and it also tends to reduce stress amplification inhibiting subsequent micro-cracking.

Figure 19 shows the evolution of horizontal damage (vertical micro-cracks) at the end of the triaxial compression test. In accordance with the boundary conditions, the space distribution of damage is symmetric. The final amount of horizontal damage in the sample with initial vertical cracks is similar to that in the initially undamaged sample, which means that less damage is accumulated during the test simulated with the initially damaged sample, and that stress in the sample with initial damage remains in the elastic domain for a higher axial displacement load than in the initially undamaged sample. Once vertical cracks have formed in the initially damaged sample, damage evolves in a similar way as in the sample that already contained vertical cracks. The sample with initial vertical damage (horizontal micro-cracks) is more compliant in the vertical direction (i.e., the Young's modulus E_1 is initially smaller than in the other samples). Loading is controlled in displacement. Therefore, the sample with initial vertical damage develops less internal stress than in the other samples, and remains in elasticity for a higher axial displacement load. As a result, the horizontal damage cumulated in the sample with initial vertical damage is almost zero except at the edges. Overall, the intensity of deformation throughout the sample follows a similar distribution in the three samples. The space distribution of horizontal damage in Figure 19 explains the space distribution of horizontal deformation in Figure 20: a higher increment of horizontal damage calculated during the test leads to higher horizontal irreversible deformation, and therefore, higher horizontal total deformation. It follows that horizontal deformation in the sample with no initial damage is higher that in the sample with initial horizontal damage, which is itself higher than that in the sample with initial vertical damage.

In a core that contains vertical cracks, the plug modeled here with initial vertical cracks can represent a sample cored in the axial direction of the core, and the plug containing initial horizontal cracks can represent a sample cored in the transversal direction of that core. Therefore, the numerical results above indicate that plugs extracted from the same core in two orthogonal directions can exhibit very different stress-strain responses: a high compression strength is expected for the plug cored in the transversal direction, whereas a low compression strength is expected for the plug cored along the axis of the core. The DSID model can be used to characterize intrinsic mechanical

anisotropy from induced damage anisotropy. A sample containing one family of vertical cracks subject to vertical compression can be seen as the equivalent of a sample containing a family of horizontal cracks subject to lateral compression. Therefore, experiments on samples with different states of initial damage can be done to test three-dimensional states of stress with triaxial compression cells, and modeling initial damage allows predicting the behavior of anisotropic rock under different states of differential stress.

Influence of delamination planes on damage propagation

The influence of a horizontal bedding delamination plane on damage propagation within a whole core sample (101.6 mm in diameter, 152.4 mm in height) was studied with two different numerical models (Figure 21):

- A discrete fracture model: at mid-height of the sample, a discontinuity was introduced. The top and bottom parts of the sample were debonded. At the interface, a non-penetration condition was adopted in the normal direction, and a friction law (Figure 9) was used in the tangential directions, with a friction coefficient of 0.8 (note that in real geological conditions, this coefficient varies largely with the type of fracture surface and gouge material in the fracture).
- A smeared damaged zone: a 5 mm thick layer of initially damaged Finite Elements ($\Omega_{11} = 0.2$) is introduced in the middle of the shale sample.

During the axial compression phase, a vertical strain of 1% was imposed under a constant confining stress of 4,000 psi (27.6 MPa). As noted previously, stress concentrations occur near the contact surfaces between the steel platens and the rock sample, due to friction. In the discrete fracture model, sliding can occur once friction at the interface between the top and bottom parts of the sample exceeds its frictional strength. Compared to a linear elastic model (Figure 22a), contact properties introduced in the discrete crack model (Figure 22b) constrain the material at the crack surfaces, which results in slightly higher stress. Overall results in the homogeneous sample (Figure 22a) are similar to those in the sample containing a horizontal discrete fracture

(Figure 22b), because the fracture is closed during the axial compression phase. By contrast, the behavior of a plug containing a uniform distribution of initial horizontal micro-cracks (Figure 20c) differs from that of a plug that is initially undamaged (Figure 20a), because the DSID model assumes that closed horizontal-microcracks affect stiffness in the same way as open horizontal micro-cracks. In order to account for the increase of compression strength during crack closure, a unilateral condition would have to be added in the DSID model (Chaboche 1993). In the test with a smeared damaged zone (Figure 22c, the stiffness tensor decreases only in the zone that contains micro-cracks, due to damage propagation. As expected, internal stress developed in the sample is lower than in the linear elastic test. The main difference with the discrete fracture case is the presence of stress concentrations near the damaged zone. The delamination results indicate that the DSID model can be used to approximate discrete features. However, the triaxial stress-strain calibration approach is based on capturing the effect of crack generating processes. If the model is used for discrete crack-closing processes, then stiffness evolution should instead be calibrated to experiments on fracture closing and asperity weakening (e.g., considering Hertzian contact theory).

The evolution of the energy dissipation provides a way to analyze the physical processes, such as crack opening and crack debonding, which dominate damage propagation before failure. Figures 23 and 24 show the energy dissipated in the smeared damaged zone due to the accumulation of irreversible deformation (induced by crack opening: W_{irr}) and due to crack debonding (W_d):

$$W_{irr} = \int \boldsymbol{\sigma} : \dot{\boldsymbol{\varepsilon}}^{id} \, \mathrm{d}t \tag{18}$$

$$W_d = \int \mathbf{Y} : \dot{\boldsymbol{\Omega}} \, \mathrm{d}t \tag{19}$$

Energy dissipation starts at the external boundary of the sample and propagates towards the center. Finite Elements close to the boundary experience less confinement than the elements in the center, which results in higher deformation close to the lateral boundary. The space distribution of the energy dissipated by crack debonding is similar to that of the energy dissipated by irreversible deformation.

CONCLUSION

A Continuum Damage Mechanics model, named the Differential Stress Induced Damage (DSID) model, was formulated by two of the authors in order to capture the anisotropy of rock deformation and stiffness induced by tensile stress differences. This model was calibrated against laboratory data obtained during triaxial compression tests performed on Bakken shale, by using an optimization technique to match the stress-strain behavior.

- The triaxial compression test used for model calibration was simulated for different sample sizes with ABAQUS finite element software. The effects of sample size on stress concentrations and damage localization, and the anisotropy induced by microscopic crack propagation in initially isotropic and anisotropic shale samples is captured by the DSID model. The non uniform state of stress reached after the axial loading stage in elements located in the central zone of the mesh reveals boundary effects.
- Overall, stress-strain curves obtained with the Finite Element Method match the stress-strain curves obtained with the one-element model used for calibration, which justifies the use of the DSID model to study stress-induced anisotropy at multiple scales.
- When considering different states of initial damage representing thin laminae, the anisotropy index grows faster in the plug tests simulated for samples with initial horizontal damage (i.e., initial vertical micro-cracks).
- The influence of a horizontal bedding delamination plane located at mid-height of a linear elastic shale sample was studied by using a discrete fracture model and a smeared damage zone model. The evolution of the energy dissipation rate in the sample illustrates two main differences between the two numerical models: First, the CDM smear zone model predicts vertical weakening in the damage zone that is not included with the hard normal contact option of the discrete surface model. Second, the discrete fracture model uses a sliding friction threshold that is not exceeded under axial loading, whereas the CDM zone predicts strain localization, gradual energy dissipation and further material weakening at the delamination interface.

This numerical study of damage anisotropy and damage propagation demonstrates the utility of the DSID model to simulate realistic rock deformation using a common laboratory testing configuration. Although a simple scenario was considered, results suggest that the model is suitable for a range of engineering and geologic problems where anisotropic mechanical properties are expected. The model will be further enhanced by plastic coupling so that the full stress-strain and failure response can be modeled, and by coupling of pressurization damage to fluid flow, for future applications in hydraulic fracturing simulation. Future work will be dedicated to the coupled simulation of fracture and damaged zone propagation, which could allow predicting rock strength and failure subsequent to micro-crack propagation.

ACKNOWLEDGMENTS

This research was performed in the School of Civil and Environmental Engineering at the Georgia Institute of Technology, with the support of *ConocoPhillips* on a project entitled "Finite Element Modeling of Hydraulic Fracturing".

REFERENCES

Abaqus 6.9 Documentation. SIMULIA, Dassault Systemes, Providence, Rhode Island, <http://www.3ds.com/products-services/simulia/portfolio/abaqus/>.

Abu Al-Rub, R. K. and Kim, S.-M. (2010). "Computational applications of a coupled plasticity-damage constitutive model for simulating plain concrete fracture.." *Engineering Fracture Mechanics*, 77, 1577–1603.

Adachi, J., Siebrits, E., Peirce, A., and Desroches, J. (2007). "Computer simulation of hydraulic fractures." *International Journal of Rock Mechanics and Mining Sciences*, 44, 739–757.

Amendt, D., Busetti, S., and Wenning, Q. (2013). "Mechanical characterization in unconventional reservoirs: A facies-based methodology." *Petrophysics*, 54(5), 457–464.

Arson, C. (2009). "Etude théorique et numérique de l'endommagement thermo-hydro-mécanique des milieux poreux non saturés." Ph.D. thesis, Ecole Nationale des Ponts et Chaussées, Paris (Sept.).

Arson, C. (2014). "Generalized stress variables in continuum damage mechanics." *Mechanics Research Communications*, DOI: 10.1016/j.mechrescom.2014.06.006.

Arson, C. and Gatmiri, B. (2008). "On damage modelling in unsaturated clay rocks." *Physics and Chemistry of the Earth*, 33.

Arson, C. and Pereira, J.-M. (2013). "Influence of damage on pore size distribution and permeability of rocks." *International Journal for Numerical and Analytical Methods in Geomechanics*, 37, 810–831.

Arson, C., Xu, H., and Chester, F. (2012). "On the definition of damage in time-dependent healing models for salt rock." *Géotechnique Letters*, DOI: 10.1680/geolett.12.00013.

Bahat, D., Rabinovitch, A., and Frid, V. (2005). *Tensile Fracturing in Rocks: Tectonofractographic and Electromagnetic Radiation Methods*. Springer.

Bakhtiary, E., Xu, H., and Arson, C. (2014). "Probabilistic optimization of a continuum mechanics model to predict differential stress-induced damage in claystone." *International Journal of Rock Mechanics and Mining Sciences*, 16, 136–149, DOI: 10.1016/j.ijrmms.2014.02.015i.

665 Busetti, S., Mish, K., and Reches, Z. (2012). "Damage and plastic deformation of reservoir rocks:
666 Part 1. damage fracturing." *AAPG bulletin*, 96(9), 1687–1709.
667 Busetti, S., Xu, H., and Arson, C. (2014). "Simulation of anisotropic rock damage for geologic
668 fracturing." *Proc. of the 2014 AGU Fall Meeting*, number MR23A-4313.
669 Butt, S. and Calder, P. (1998). "Experimental procedures to measure volumetric changes and mi-
670 croseismic activity during triaxial compression tests." *International Journal of Rock Mechanics*
671 *and Mining Sciences*, 35(2), 249–254.
672 Carrier, B. and Granet, S. (2012). "Numerical modeling of hydraulic fracture problem in permeable
673 medium using cohesive zone model." *Engineering fracture mechanics*, 79, 312–328.
674 Chaboche, J.-L. (1993). "Development of continuum damage mechanics for elastic solids sustain-
675 ing anisotropic and unilateral damage." *International Journal of Damage Mechanics*, 2, 311–
676 329.
677 Cicekli, U., Voyiadjis, G. Z., and Abu Al-Rub, R. K. (2007). "A plasticity and anisotropic damage
678 model for plain concrete.." *International Journal of Plasticity*, 23, 1874–1900.
679 Colovos, J., Brannon, R., and Pinsky, P. (2013). "Reduction of macroscale calibration exper-
680 iments through constraints on anisotropic elastic stiffnesses." the 47th US Rock Mechan-
681 ics/Geomechancis Symposium, San Francisco, California (23-26 June).
682 Cowin, S. C. (1985). "The relationship between the elasticity tensor and the fabric tensor." *Me-*
683 *chanics of Materials*, 4, 137–147.
684 Crawford, A. and Wylie, D. (1987). "A modified multiple failure state triaxial testing method."
685 28th US Symposium on Rock Mechanics, Tucson, Arizona (29 June–1 July).
686 Desai, C. S. (2000). *Mechanics of materials and interfaces: The disturbed state concept*. CRC
687 press.
688 Desai, C. S. (2015). "Constitutive modeling of material and contacts using the disturbed state
689 concept: Part 1 - background and analysis." *Computers and Structures*, 146, 214–233.
690 Desai, C. S., Basaran, C., and Zhang, W. (1997). "Numerical algorithms and mesh dependence
691 in the disturbed state concept." *International Journal for Numerical Methods in Engineering*,

692 3059–3083.

693 Deudé, V., Dormieux, L., Kondo, D., and Maghous, S. (2002a). “Micromechanical Approach to
694 Nonlinear Poroelasticity : Application to Cracked Rocks.” *Journal of Engineering Mechanics*,
695 128(8), 848–855.

696 Deudé, V., Dormieux, L., Kondo, D., and Pensée, V. (2002b). “Propriétés élastiques non linéaires
697 d ’ un milieu mésofissuré.” *C.R. Mécanique, Acad. Sci. Paris*, 330, 587–592.

698 Dormieux, L., Kondo, D., and Ulm, F. (2006). *Microporomechanics*. John Wiley & Sons.

699 Dufour, N., Wong, H., Arson, C., Deleruyelle, F., and Pereira, J.-M. (2012). “A thermodynamically
700 consistent framework for saturated viscoplastic rock-materials subject to damage.” *Mechanics*
701 *Research Communications*, 45, 15–21.

702 Economides, M. and Valko, P. (1994). “Interpretation and modeling of hydraulic frcturing phe-
703 nomena with continuum damage mechanics - An application to engineering design.” *Computer*
704 *Methods and Advances in Geomechanics*, 1579–1584.

705 Elleithy, W. M., Al-Gahtani, H. J., and Tanaka, M. (2001). “Iterative coupling of bem and fem for
706 the solution of elasto-plastic fracture mechanics problems.” *Transactions of JASCOME*.

707 Faulkner, D. R., Mitchell, T. M., Healy, D., and Heap, M. J. (2006). “Slip on ’weak’ faults by the
708 rotation of regional stress in the fracture damage zone..” *Nature*, 444(7121), 922–5.

709 Frémond, M. and Nedjar, B. (1996). “Damage, gradient of damage and principle of virtual power.”
710 *International Journal of Solids and Structures*, 33, 2294–2306.

711 Gaede, O., Karrech, A., and Regenauer-Lieb, K. (2013). “Anisotropic damage mechanics as a
712 novel approach to improve pre-and post-failure borehole stability analysis.” *Geophysical Journal*
713 *International*, ggt045.

714 Ghabezloo, S., Sulem, J., Gu˜edon, S., Martineau, F., and Sant-Marc, J. (2008). “Poromechanical
715 behavior of hardened cement paste under isotropic loading.” *Cement and Concrete Research*,
716 38, 1424–1437.

717 Goodman, R. E. (1989). *Introduction to Rock Mechanics*. John Wiley & Sons, 2nd edition.

718 Halm, D. and Dragon, A. (2002). “Modelisation de l’endommagement par mesofissuration du

719 granite." *Revue Francaise de Genie Civi.*, 17, 21–33.

720 Hamiel, Y., Liu, Y., Lyakhovsky, V., Ben-Zion, Y., and Lockner, D. (2004a). "A viscoelastic dam-
721 age model with applications to stable and unstable fracturing." *Geophysical Journal Interna-*
722 *tional*, 159(3), 1155–1165.

723 Hamiel, Y., Lyakhovsky, V., and Agnon, A. (2004b). "Coupled evolution of damage and porosity
724 in poroelastic media: theory and applications to deformation of porous rocks." *Geophysical*
725 *Journal International*, 156(3), 701–713.

726 Hayakawa, K. and Murakami, S. (1997). "Thermodynamical modeling of elastic-plastic damage
727 and experimental validation of damage potential." *International Journal of Damage Mechanics*,
728 6, 333–363.

729 Healy, D. (2008). "Damage patterns, stress rotations and pore fluid pressures in strike-slip fault
730 zones." *Journal of Geophysical Research*, 113(B12), 1–16.

731 Heap, M. J., Faulkner, D. R., Meredith, P. G., and Vinciguerra, S. (2010). "Elastic moduli evo-
732 lution and accompanying stress changes with increasing crack damage: implications for stress
733 changes around fault zones and volcanoes during deformation." *Geophysical Journal Interna-*
734 *tional*, 183(1), 225–236.

735 Homand-Etienne, F., Hoxha, D., and Shao, J. F. (1998). "A Continuum Damage Constitutive Law
736 for Brittle Rocks." *Computers and Geotechnics*, 22(2), 135–151.

737 Horii, H. and Nemat-Nasser, S. (1986). "Brittle failure in compression: splitting, faulting and
738 brittle-ductile transition." *Philosophical Transactions of the Royal Society of London. Series A,*
739 *MAthematical and Physical Science*, 319(1549), 337–374.

740 Jin, W., Xu, H., Arson, C., and Busetti, S. (2016). "Computational model coupling mode ii dis-
741 crete fracture propagation with continuum damage zone evolution." *International Journal for*
742 *Numerical and Analytical Methods in Geomechanics*.

743 Kachanov, M. (1992). "Effective elastic properties of cracked solids: critical review of some basic
744 concepts." *Appl. Mech. Rev.*, 45(8), 304–335.

745 Katz, O. and Reches, Z. (2004). "Microfracturing, damage, and failure of brittle granites." *Journal*

of Geophysical Research: Solid Earth, 109(B1), n/a–n/a.

Kondo, D. and Dormieux, L. (2004). "Approche micro-mécanique du couplage permabilité - endommagement." *Comptes-Rendus de Mécanique, Acad. Sci. Paris*, 332, 135–140.

Krajcinovic, D. (1996). *Damage Mechanics*. North-Holland.

Lee, J. and Fenves, G. (1998). "Plastic-damage model for cyclic loading of concrete structures." *Journal of Engineering Mechanics*, 124, 892–900.

Lemaître, J. and Desmorat, R. (2005). *Engineering Damage Mechanics. Ductile, creep, fatigue and brittle failure.* Springer - Verlag, Berlin Heidelberg.

Liu, H. W. (1984). "On the fundamental basis of fracture mechanics." *Engineering Fracture Mechancis*, 17(5), 425–438.

Lu, Y. and Elsworth, D. (2012). "Combined Microscopic-Macroscopic Modeling of Rock Damage and Failure." *46th Rock Mechanics Geomechanics Symposium*, Chicago, IL, ARMA 12–250.

Lubarda, V. and Krajcinovic, D. (1993). "Damage tensors and the crack density distribution." *International Journal of Solids and Structures*, 30(20), 2659–2677.

Lubliner, J., Oliver, J., Oller, S., and Onate, E. (1989). "A platic-damage model for concrete." *International Journal of Solids and Structures*, 23(3), 299–326.

Lyakhovsky, V., Reches, Z., Weinberger, R., and Scott, T. E. (1997). "Non-linear elastic behaviour of damaged rocks." *Geophysical Journal International*, 130(1), 157–166.

Lydzba, D. and Shao, J. (2000). "Study of poroelasticity material coefficients as response of microstructure." *Mechanics of Cohesive-Frictional Materials*, 5, 149–171.

Maleki, K. and Pouya, A. (2010). "Numerical simulation of damage–Permeability relationship in brittle geomaterials." *Computers and Geotechnics*, 37(5), 619–628.

MATLAB. MathWorks, Natick, Massachusetts, <http://www.mathworks.com/products/matlab/>.

Mazars, J. (1986). "A description of micro- and macro scale damage of concrete structures." *Engineering Fracture Mechancis*, 25(5–6), 729–737.

Mazars, J. and Pijaudier-Cabot, G. (1989). "Continuum damage theory - application to concrete.." *Journal of Engineering Mechanics*, 115(2), 345–365.

Mohammadi, S. (2007). *Extended Finite Element Method for Fracture Analysis of Structures*. Blackwell.

Nelson, R. (2001). *Geologic Analysis of Naturally Fractured Reservoirs*. Gulf Professional Publishing, 2nd edition.

Oda, M. (1984). "Similarity rules of crack geometry in statistically homogeneous rock masses." *Mechanics of Materials*, 3, 119–129.

Ortiz, M. (1985). "A constitutive theory for the inelastic behaviour of concrete." *Mech. Mater.*, 4, 67–93.

Pagoulatos, A. (2004). "Evalutaion of multistage triaxial testing on berea sandstone." M.S. thesis, University of Oklahoma., Oklahoma.

Paterson, M. (1978). *Experimental Rock Deformation: The Brittle Field*. Springer Verlag, New York.

Pereira, J.-M. and Arson, C. (2013). "Retention and permeability properties of damaged porous rocks." *Computers & Geotechnics*, 48, 272–282.

Ramurthy, M., Barree, R. D., Broacha, E., Longwell, J. D., Kundert, D. P., and Tamayo, C. (2009a). "Effects of high process-zone stress in shale stimulation treatments." Rocky Mountain Petroleum Technology, Denver, Colorado, USA,.

Ramurthy, M., Lyons, B., Hendrickson, R. B., Barree, R. D., and Magill, D. P. (2009b). "Effects of high pressure-dependent leakoff and high process-zone stress in coal-stimulation treatments." *SPE journal*, 24(3), 407–414.

Raveendra, S. and Cruse, T. (2005). "Bem analysis of problems of fracture mechanics." *Developments in Boundary Element Methods: Industrial applications*, 5, 182.

Savitski, A. and Detournay, E. (2002). "Propagation of a penny-shaped fluid-driven fracture in an impermeable rock: asymptotic solutions." *International Journal of Solids and Structures*, 39, 6311–6337.

Shalev, E. and Lyakhovsky, V. (2013). "The processes controlling damage zone propagation induced by wellbore fluid injection." *Geophysical Journal International*, 193(1), 209–219.

Shao, J. (1998). "Poroelastic behaviour of brittle rock materials with anisotropic damage." *Mechanics of Materials*, 30(1), 41–53.

Shao, J., Zhou, H., and Chau, K. (2005). "Coupling between anisotropic damage and permeability variation in brittle rocks.." *International Journal for Numerical and Analytical Methods i Geomechanics*, 29(12), 1231 – 1247.

Shao, J.-F. and Lydzba, D. (1999). "Un modèle d'endommagement poroélastique pour milieux poreux saturés." *C.R. Acad. Sci. Paris*, 327, 1305–1310.

Shen, X. (2012). "Modeling Fractures with Continuum Damage and Its Numerical Application to Stimulation Estimates." *46th Rock Mechanics Geomechanics Symposium*, Chicago, IL, ARMA 12–196.

Shlyapobersky, J. and Chudnovsky, A. (1994). "Review of recent developments in fracture mechanics with petroleum engineering applications." Rock Mechanics in Petroleum Engineering, 29-31 August, Delft, Netherlands, Society of Petroleum Engineers.

Smart, K., Ofoegbu, G., Das, K., and Basu, D. (2012). "Geomechanical Modeling of Hydraulic Fracture Initiation and Propagation in a Mechanically Stratified Geologic System." *46th Rock Mechanics Geomechanics Symposium*, Chicago, IL, ARMA 12–275.

Suzuki, T. (2012). "Understanding of dynamic earthquake slip behavior using damage as a tensor variable: Microcrack distribution, orientation, and mode and secondary faulting." *Journal of Geophysical Research*, 117(B5), 1–20.

Swoboda, G. and Yang, Q. (1999a). "An energy-based damage model of geomaterials -II. Deduction of damage evolution laws." *International Journal of Solids and Structures*, 36, 1735–1755.

Swoboda, G. and Yang, Q. (1999b). "An energy-based damage model of geomaterials. I. Formulation and numerical results." *International Journal of Solids and Structures*, 36(12), 1719–1734.

Swoboda, G., Yang, Q., and Ito, F. (1995). "Damage Propagation Model and its Application to Rock Engineering Problems." *Proc. 8th Inernational Congress on Rock Mechanics*, 159–163.

Swoboda, G., Yang, Q., and Zhou, W. (1997). "An energy-based damage model and its engineering application." *Computer Methods and Advances in Geomechanics*, 1821–1828.

827 Tarokh, A. and Fakhimi, A. (2013). "Relationship between grain size and fracture properties of
828 rock." the 47th US Rock Mechanics/Geomechancis Symposium, San Francisco, California (23-
829 26 June).

830 Valko, P. and Economides, M. (1993). "A Continuum-Damage-Mechanics Model of Hydraulic
831 Fracturing." *Journal of Petroleum Technology*, 45(3), 198–205.

832 Valko, P. and Economides, M. (1994). "Propagation of Hydraulically Induced Fractures a Con-
833 tinuum Damage Mechanics Approach." *International Journal of Rock Mechanics and Mining*
834 *Sciences & Geomechanics Abstracts*, 31(3), 221–229.

835 Wu, S. and Chudnovsky, A. (1993). "Effect of microcrack array on stress intensity factor of main
836 crack." *International Journal of Fracture*, 59, 41–52.

837 Xie, N., Zhu, Q.-Z., Shao, J.-F., and Xu, L.-H. (2012). "Micromechanical analysis of damage in
838 saturated quasi brittle materials." *International Journal of Solids and Structures*, 49(6), 919–928.

839 Xu, H. and Arson, C. (2014). "Anisotropic damage models for geomaterials: Theoretical and nu-
840 merical challenges." *International Journal of Computational Methods, Special Issue on Compu-*
841 *tational Geomechanics*, 11, DOI: 10.1142/S0219876213420073.

842 Xu, H. and Prévost, J.-H. (2016). "Integration of a continuum damage model for shale with the
843 cutting plane algorithm." *International Journal for Analytical and Numerical Methods in Ge-*
844 *omechanics*.

845 Yamashita, T. (2000). "Generation of microcracks by dynamic shear rupture and its effects on
846 rupture growth and elastic wave radiation." *Geophysical Journal International*, 143(2), 395–
847 406.

848 Zhou, J., Shao, J., and Xu, W. (2006). "Coupled modeling of damage growth and permeability
849 variation in brittle rocks." *Mechanics Research Communications*, 33(4), 450–459.

850 Zhu, C. and Arson, C. (2014). "A thermo-mechanical damage model for rock stiffness during
851 anisotropic crack opening and closure." *Acta Geotechnica*, DOI: 10.1007/s11440–013–0281–0.

TABLE 1: DSID parameters calibrated for shale under 4,000 psi (27.6 MPa) confining pressure, with $E_0 = 46$ GPa, and $\nu_0 = 0.186$). The upper and lower bounds indicate the range of values considered for the parametric study on the hardening parameter C_1.

	Free energy				Damage function		
	a_1	a_2	a_3	a_4	C_0	C_1	α (-)
	GPa^{-1}	GPa^{-1}	GPa^{-1}	GPa^{-1}	MPa	MPa	-
Optimal	7.35×10^{-4}	0.121	-3.15×10^{-2}	2.39×10^{-3}	0.01	1.18	0.399
Upper bound	7.35×10^{-4}	0.121	-3.15×10^{-2}	2.39×10^{-3}	0.01	1.78	0.399
Lower bound	7.35×10^{-4}	0.121	-3.15×10^{-2}	2.39×10^{-3}	0.01	0.71	0.399

TABLE 2: Reference Young's moduli and Poisson's ratios determined from the experimental stress-strain plot obtained under a confining stress of 3,000 psi (20.7 MPa).

	Young's	Poisson's	Damage Threshold		
Tests	Modulus	Ratio	Axial Strain	Lateral Strain	Differential Stress
	GPa		%	%	MPa
Case 1	35.71	0.169	0.1045	0.0177	37.31
Case 2	37.19	0.143	0.0543	0.0078	20.19
Case 3	38.79	0.122	0.0316	0.0039	12.26

TABLE 3: Reference Young's moduli and Poisson's ratios determined from the experimental stress-strain plot obtained under a confining stress of 1,000 psi (6.9 MPa); 2,000 psi (13.8 MPa); and 3,000 psi (20.7 MPa).

Confining	Young's	Poisson's	Damage Threshold		
Stress	Modulus	Ratio	Axial Strain	Lateral Strain	Deviatoric Stress
MPa	GPa		%	%	MPa
6.9	28.34	0.172	0.2004	0.0344	56.80
13.8	32.24	0.163	0.2005	0.0328	64.64
20.7	38.79	0.122	0.0316	0.0039	12.26

List of Figures

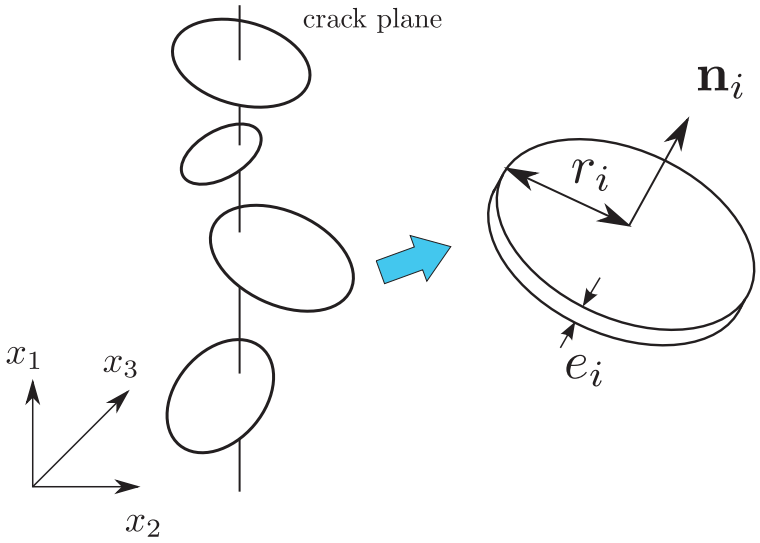

FIG. 1: Concept of Oda's fabric tensor. Each crack in the domain is represented by a penny shaped plane with thickness e_i and radius r_i. The vector normal to the plane, $\mathbf{n}_i$, provides the orientation of the crack. Modified from (Oda 1984; Arson 2009).

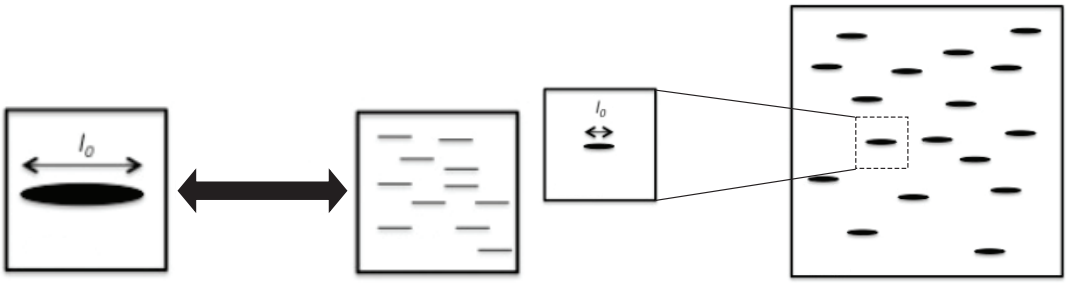

(a) REV for a family of parallel micro-cracks. (b) REV for non-interacting micro-cracks.

FIG. 2: Definition of the Representative Elementary Volume (REV) in Continuum Damage Mechanics (CDM). Example of one family of parallel micro-cracks.

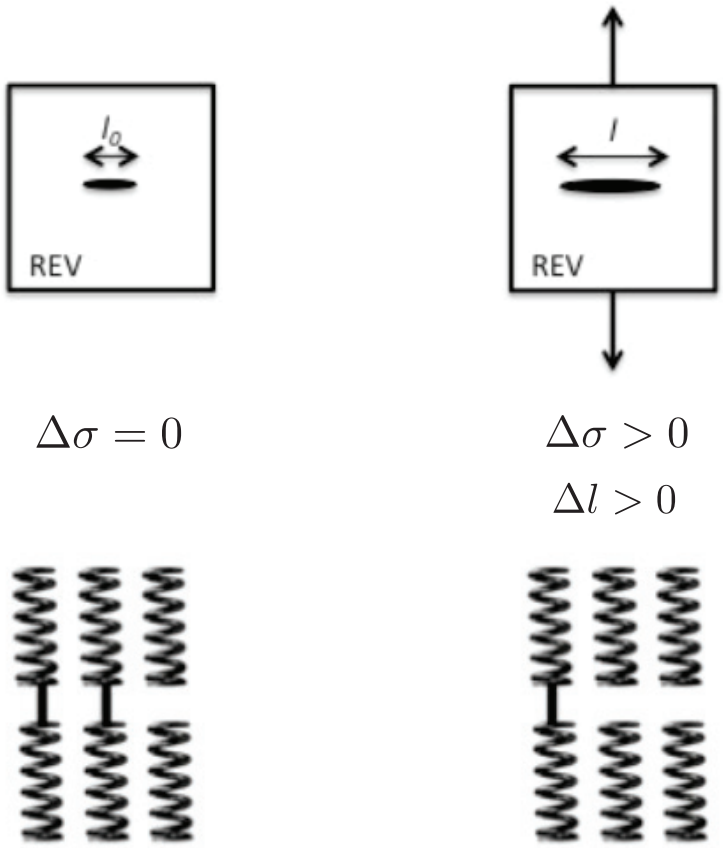

(a) Reference (initial crack) (b) Opening (larger crack)

FIG. 3: Conceptual model of stiffness for 1D tensile mesocrack propagation in mode I.

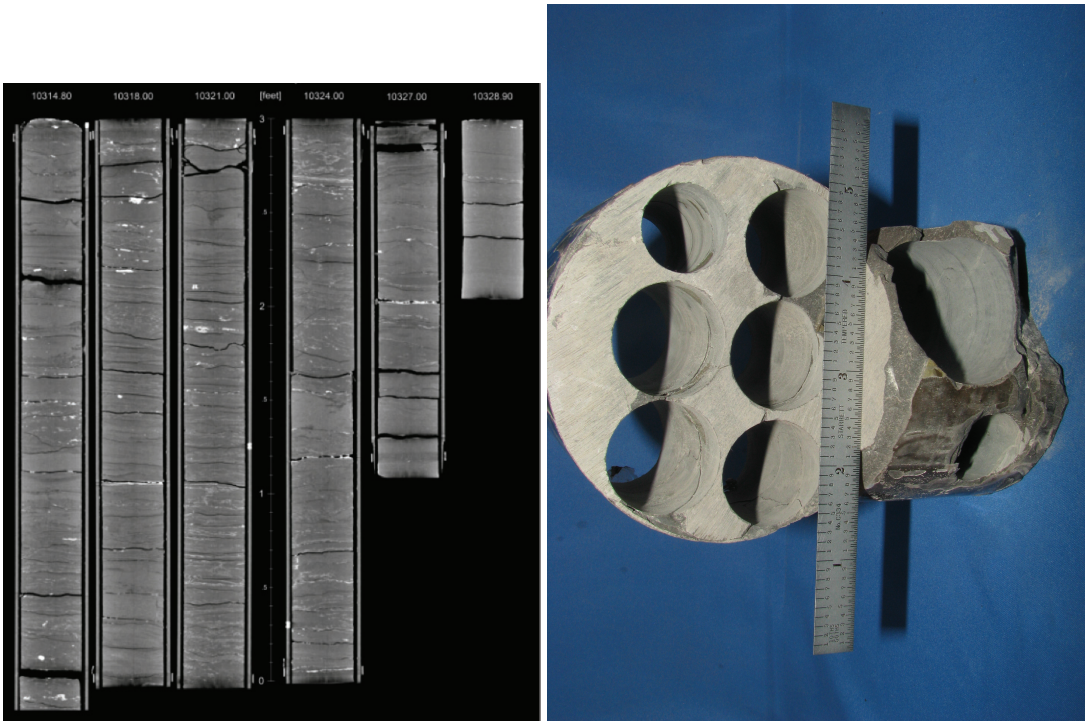

(a) CT scan photo of shale whole cores with 4 inch in diameter.

(b) Preparation of shale plugs, 1 inch in diameter and 2 inches in height.

FIG. 4: Images of Bakken shale whole core in CT scan (a) and showing a whole core bulk sample after plugging (b). From a single bulk sample at a given depth (b), multiple triaxial tests at different confining pressures were run for Mohr Coulomb characterization (Amendt et al. 2013). The present calibration dataset comes from a single bulk core sample similar to that shown in (b). *(courtesy of ConocoPhillips, Houston, TX).*

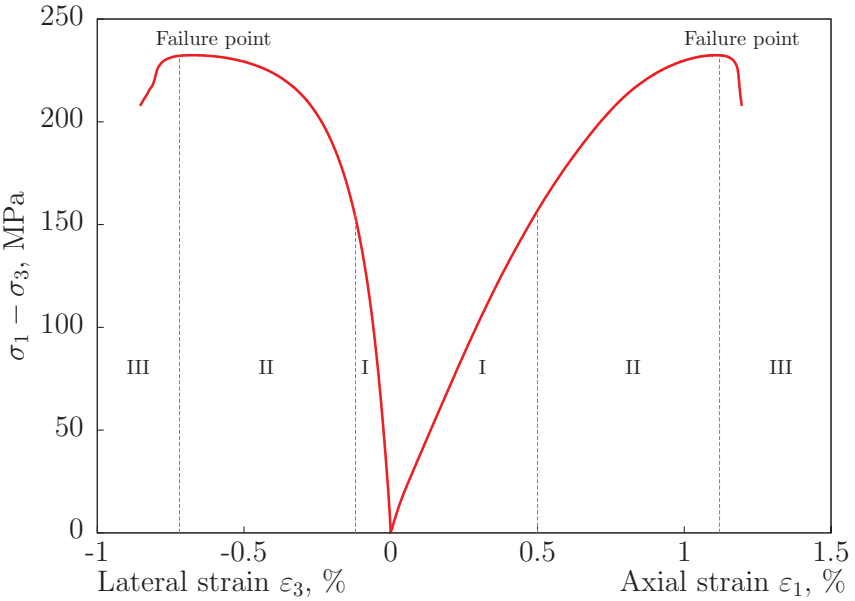

FIG. 5: Typical stress-strain curve of shale under triaxial compression: (I) Brittle deformation regime. (II) Ductile deformation regime. (III) Post-peak behavior (after failure). Modified from (Goodman 1989; Katz and Reches 2004).

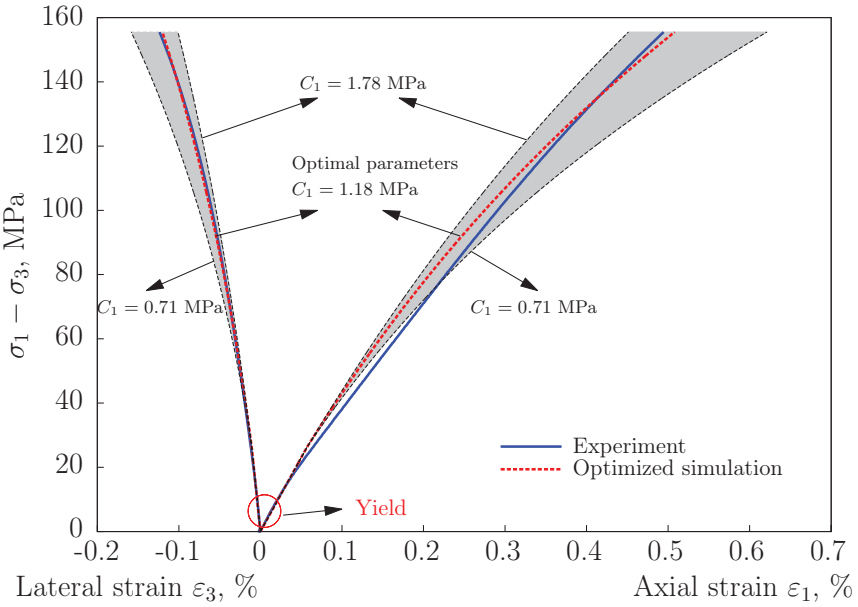

FIG. 6: Calibration of the DSID model against a triaxial compression test performed under 4,000 psi (27.6 MPa) confining stress.

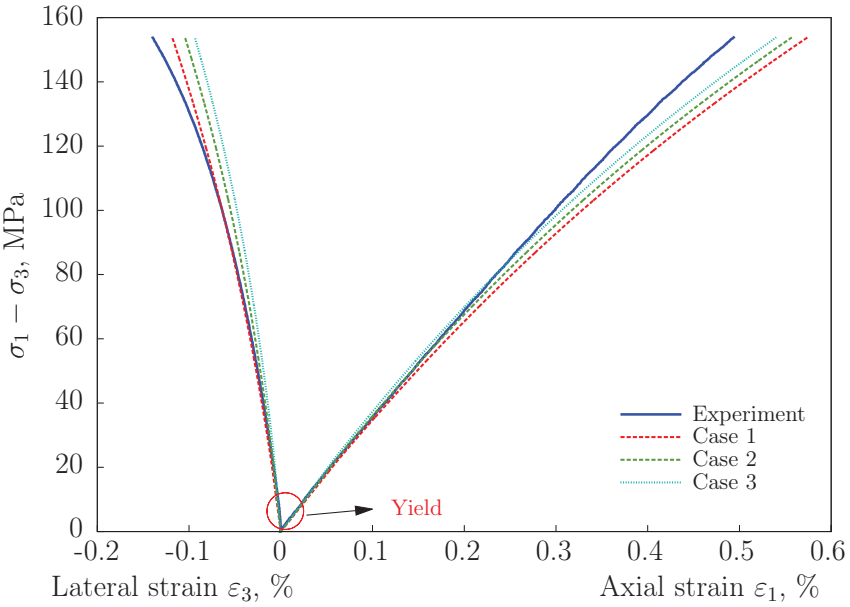

FIG. 7: Comparison between experimental and numerical stress-strain plots for the three sets of reference elastic moduli considered in the triaxial compression test performed under 3,000 psi (20.7 MPa) confining stress.

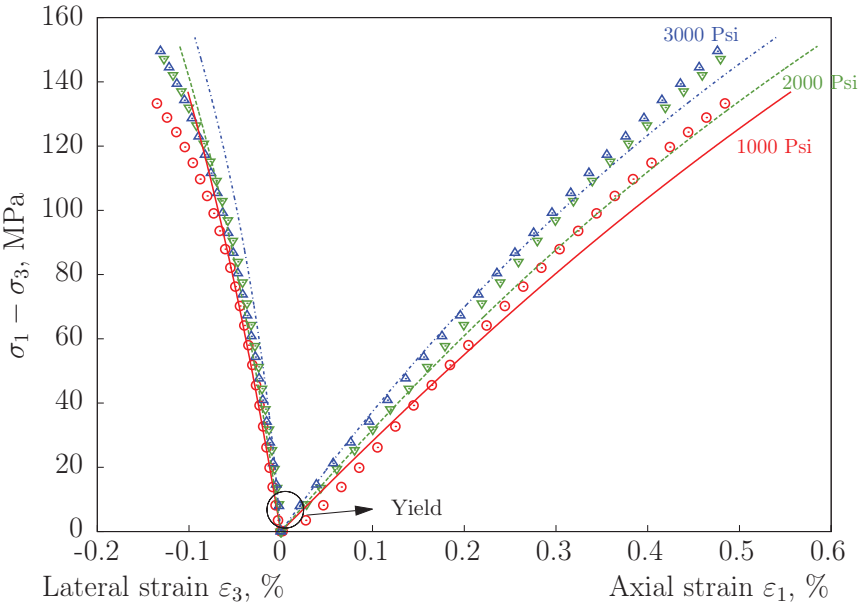

FIG. 8: Comparison between experimental and numerical stress-strain plots for the triaxial compression tests performed under 1,000 psi (6.9 MPa); 2,000 psi (13.8 MPa); and 3,000 psi (20.7 MPa) confining stress. Dots represent experimental data, and lines represent simulation results obtained with calibrated DSID parameters. Different colors are used for the different confining stresses considered.

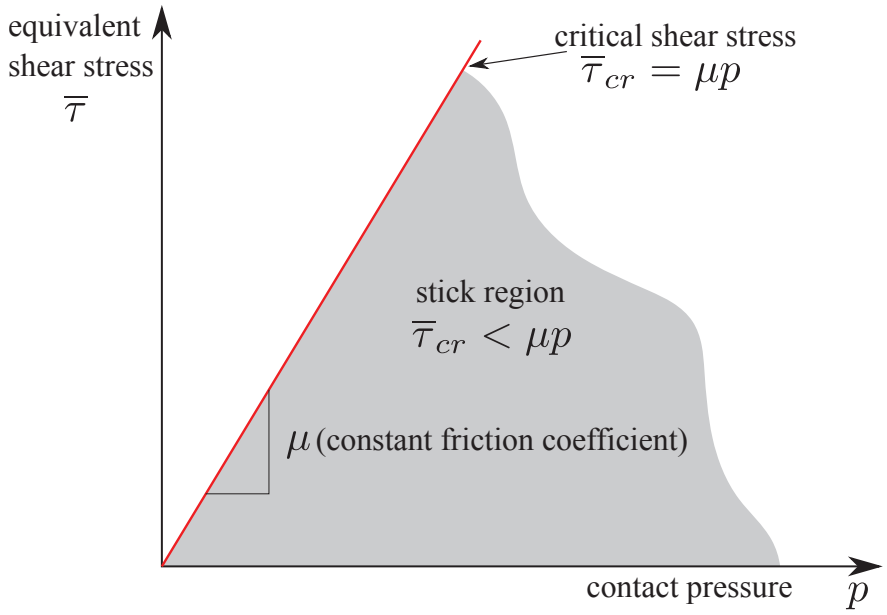

FIG. 9: Friction law governing the sliding mechanism between surfaces in contact. Modified from (Abaqus).

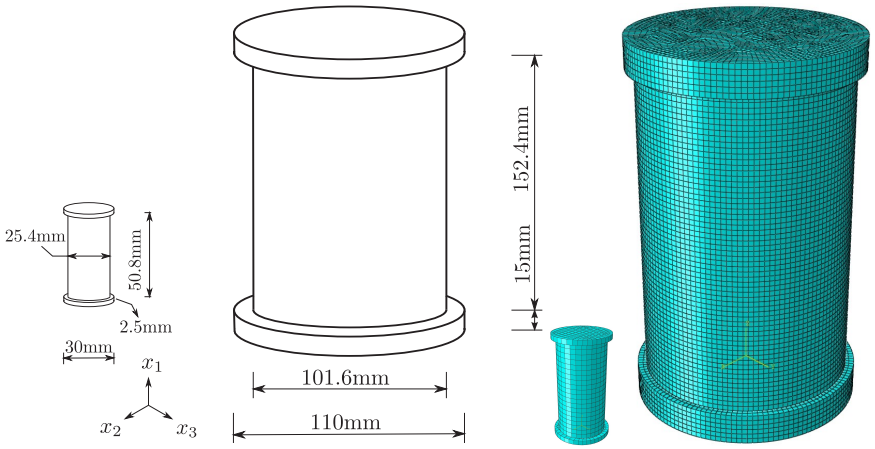

FIG. 10: Sizes of the sample modeled with the FEM: the left sketch represents the standard plug test, in which the sample is assumed to be 25.4×50.8 mm (1×2 inch); the right sketch represents a portion of a whole core, with dimensions 101.6×152.4 mm (4×6 inch). The figure on the right shows the mesh adopted in the simulations.

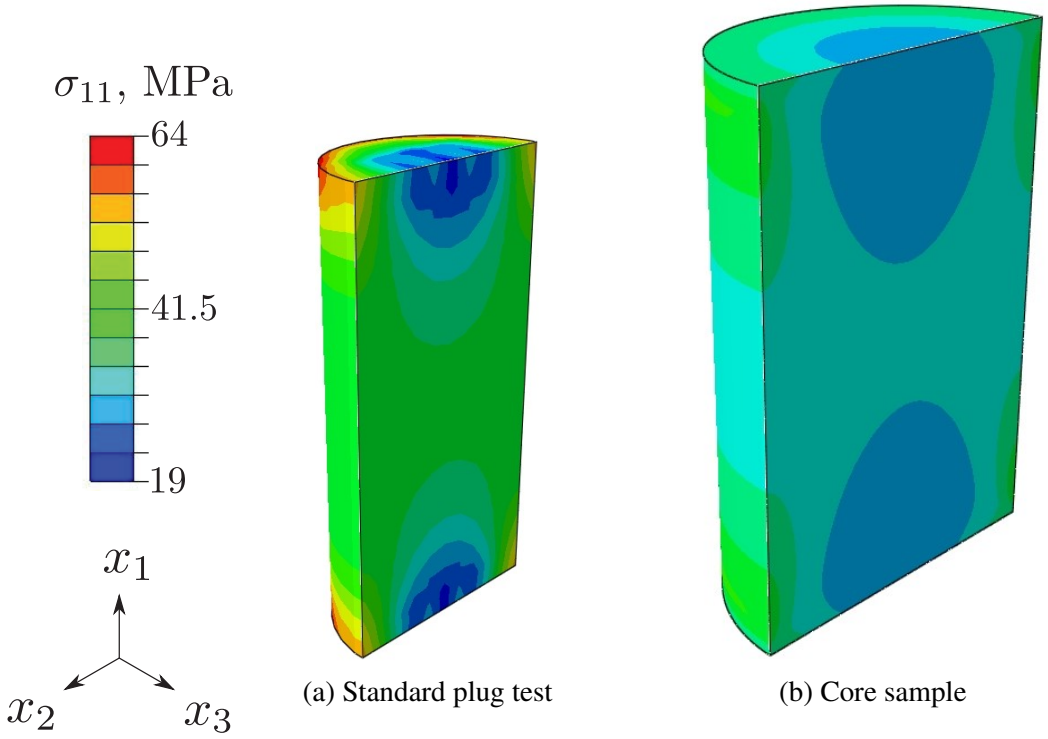

(a) Standard plug test (b) Core sample

FIG. 11: Vertical stress distribution in the plug and in the whole core sample after the confining phase (4,000 psi, i.e. 27.6 MPa).

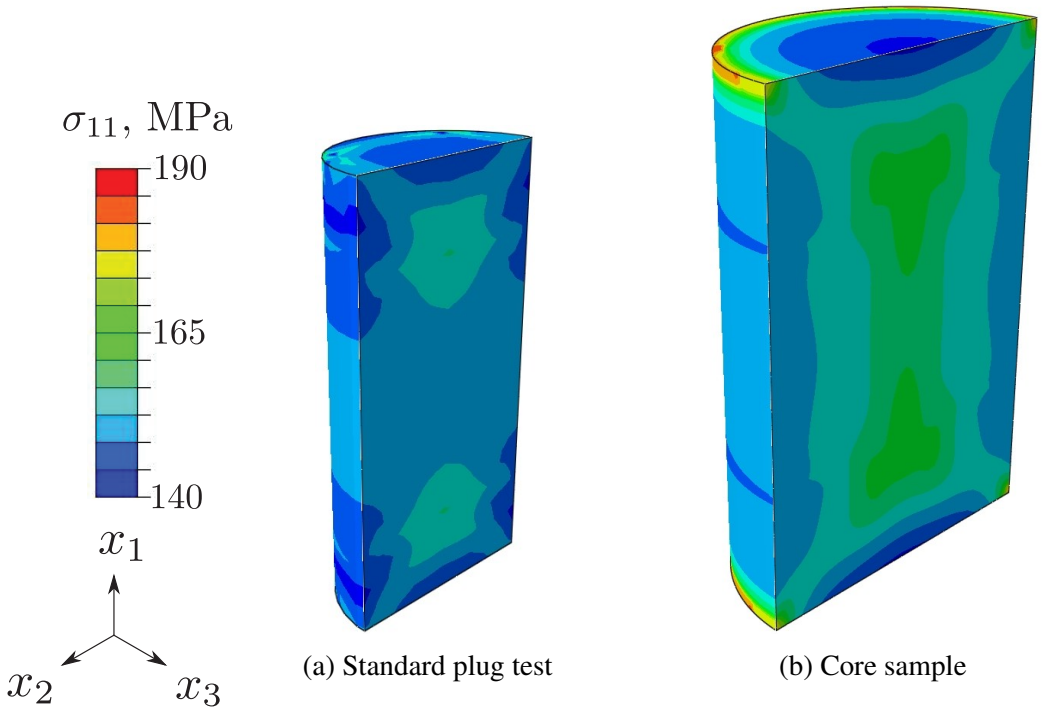

(a) Standard plug test (b) Core sample

FIG. 12: Vertical stress distribution in the plug and in the whole core sample after the axial loading phase (confining stress of 4,000 psi, i.e. 27.6 MPa).

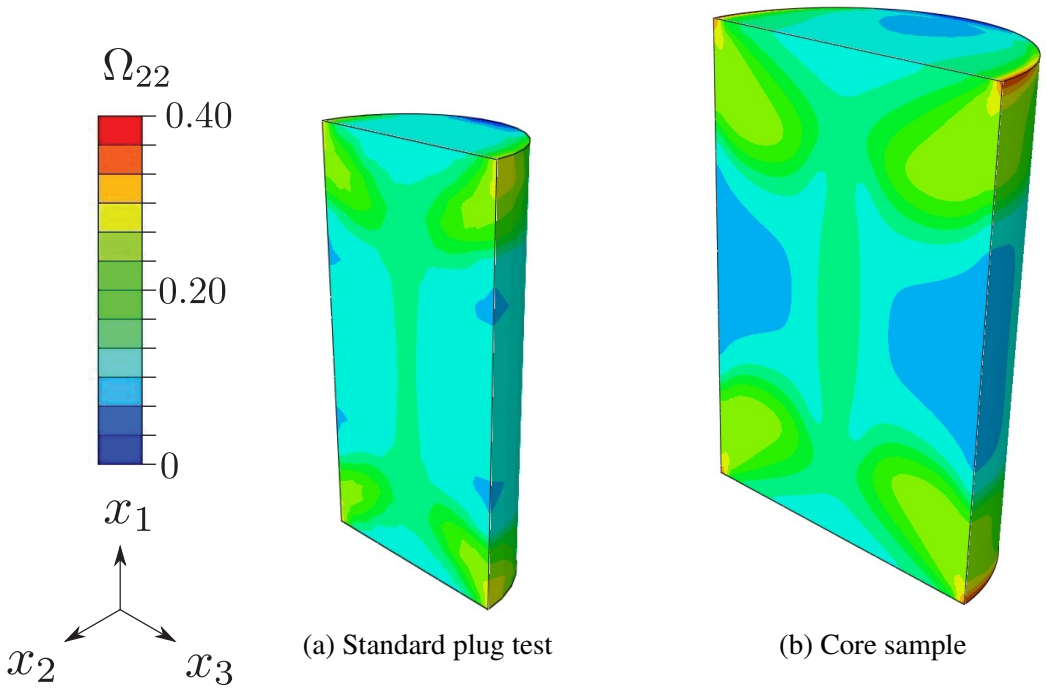

(a) Standard plug test

(b) Core sample

FIG. 13: Horizontal damage distribution (i.e. distribution of vertical cracks) in the plug and in the whole core sample, after the axial loading phase (confining stress of 4,000 psi, i.e. 27.6 MPa).

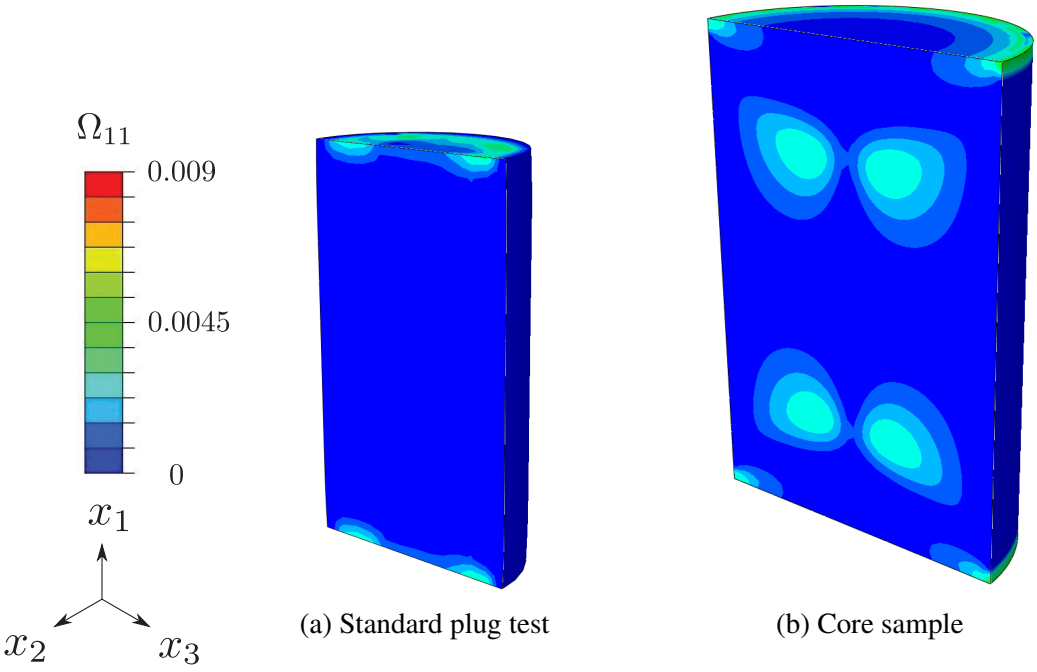

(a) Standard plug test

(b) Core sample

FIG. 14: Vertical damage distribution (i.e. distribution of horizontal cracks) in the plug and in the whole core sample, after the axial loading phase (confining stress of 4,000 psi, i.e. 27.6 MPa).

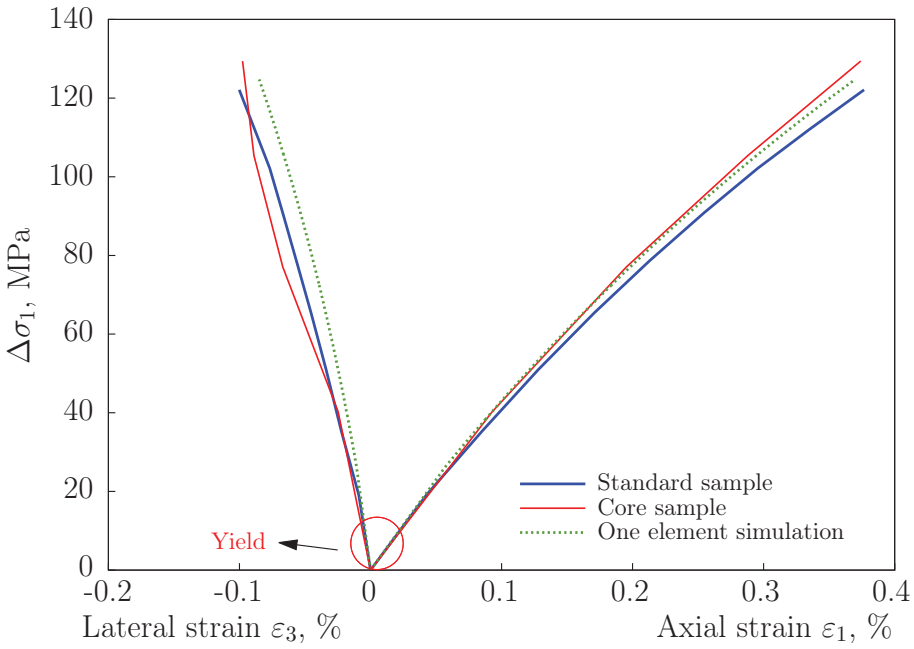

FIG. 15: Stress-strain curve obtained numerically with MATLAB (for the ideal one-element test with no edge effects) and with ABAQUS (for a central element of the mesh), for a triaxial compression test performed under 4,000 psi (27. 6 MPa) confining pressure.

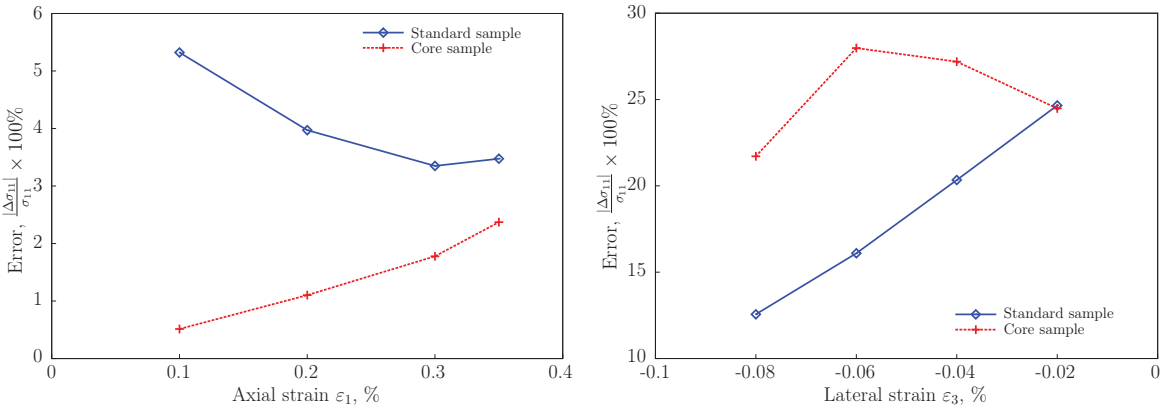

(a) Error prediction with respect to axial strain. (b) Error prediction with respect to lateral strain

FIG. 16: Error prediction for the standard sample and core sample.

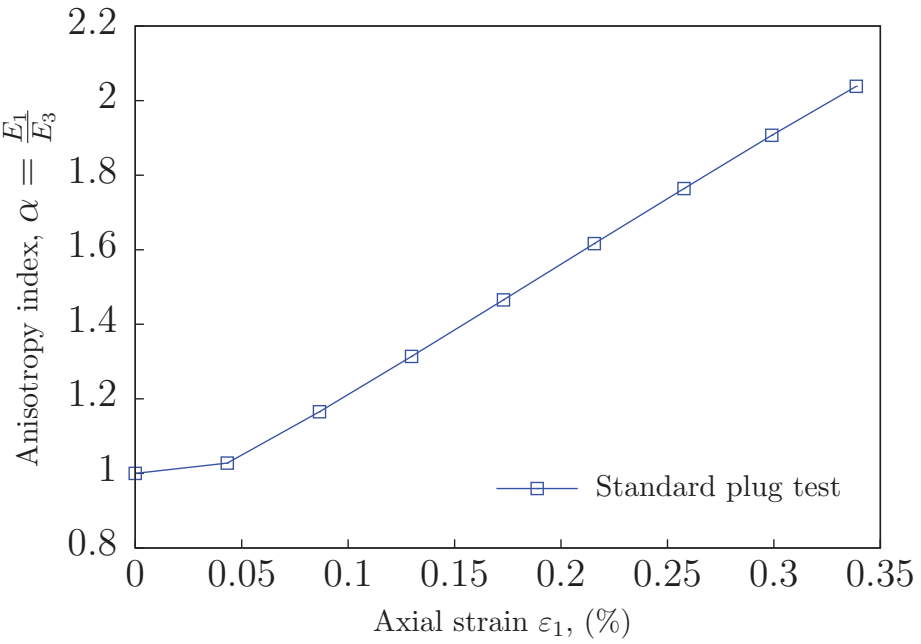

FIG. 17: Evolution of the elastic anisotropy index in the standard plug test, for an initially undamaged sample.

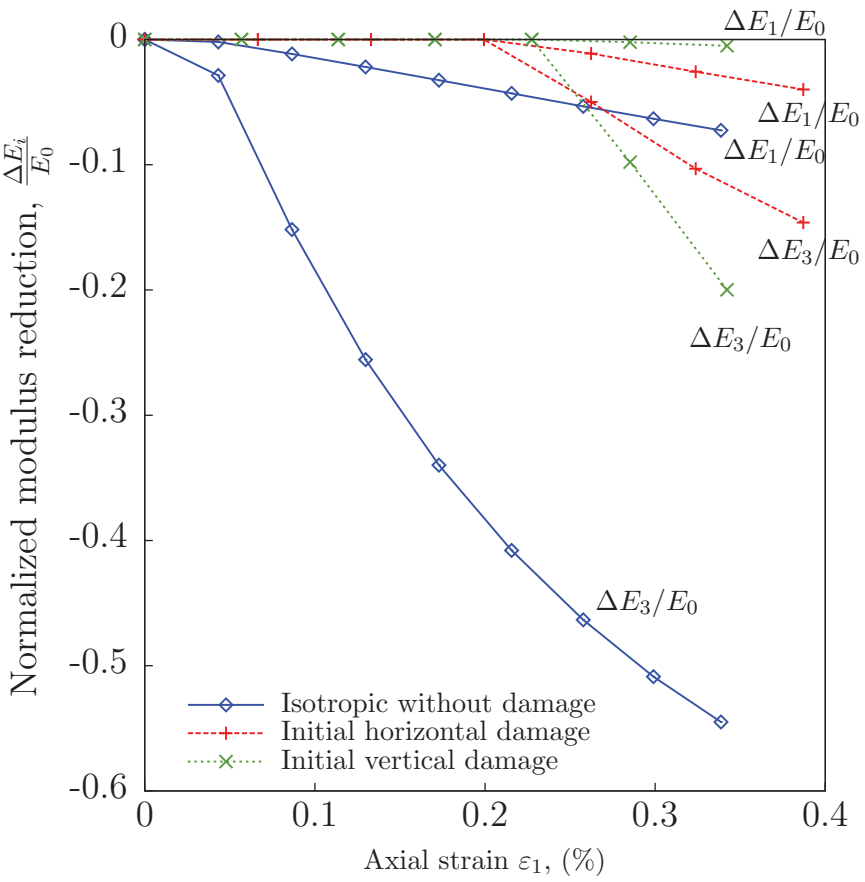

FIG. 18: Evolution of the normalized elastic moduli change with loading in the standard plug test

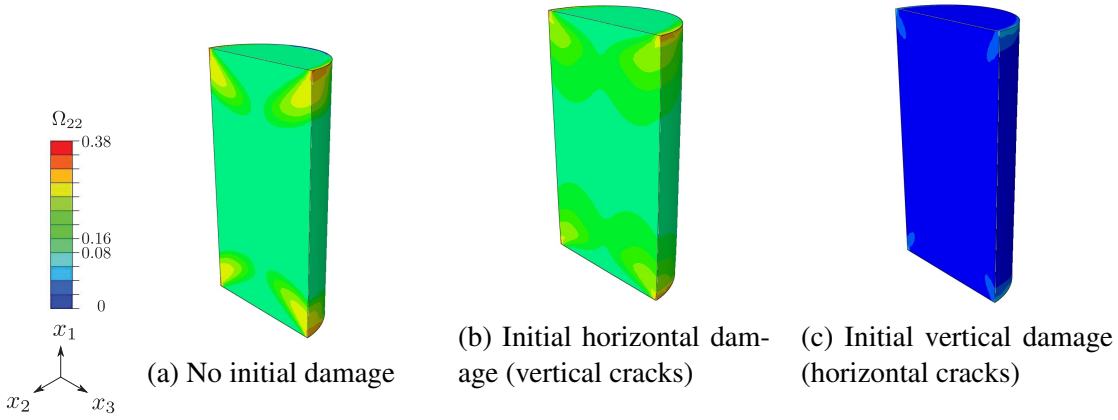

(a) No initial damage

(b) Initial horizontal damage (vertical cracks)

(c) Initial vertical damage (horizontal cracks)

FIG. 19: Horizontal damage distribution (i.e., vertical micro-cracks) after the axial loading phase.

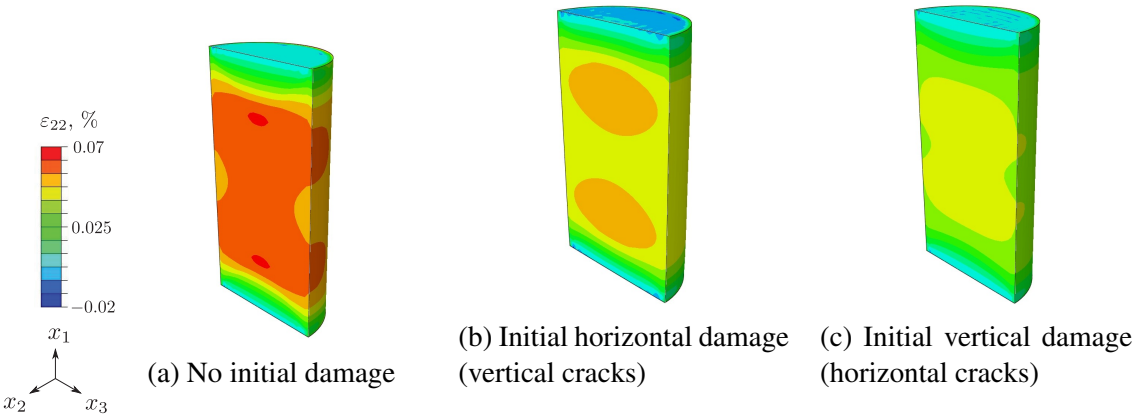

(a) No initial damage

(b) Initial horizontal damage (vertical cracks)

(c) Initial vertical damage (horizontal cracks)

FIG. 20: Horizontal strain distribution after the axial loading phase in the plug test.

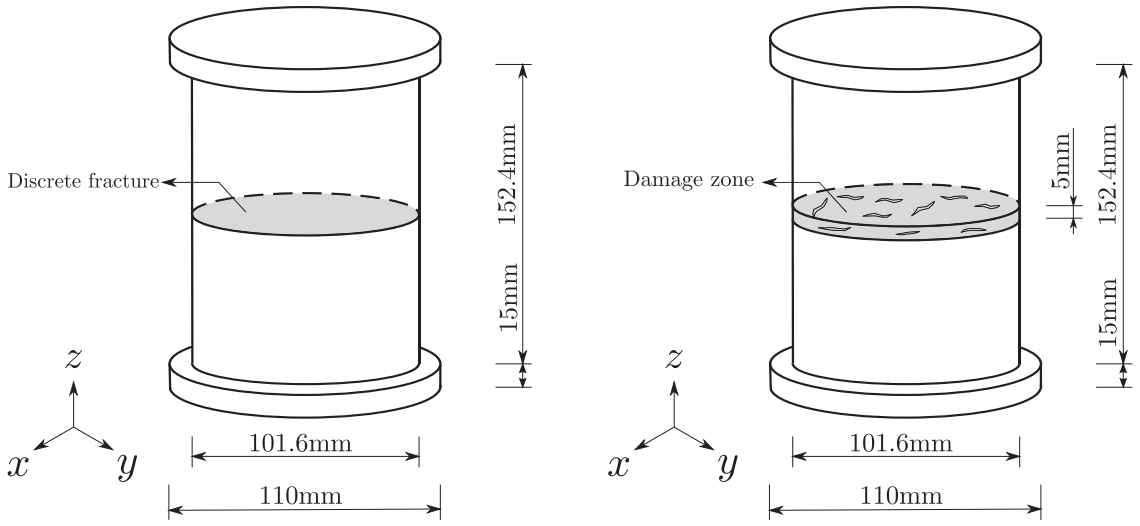

(a) Simulation domain with an embed discrete crack.

(b) Simulation domain with a smeared damage zone.

FIG. 21: Sample with a horizontal bedding delamination plane, modelied with: (a) an embedded discrete crack; and (b) an equivalent smeared damage zone.

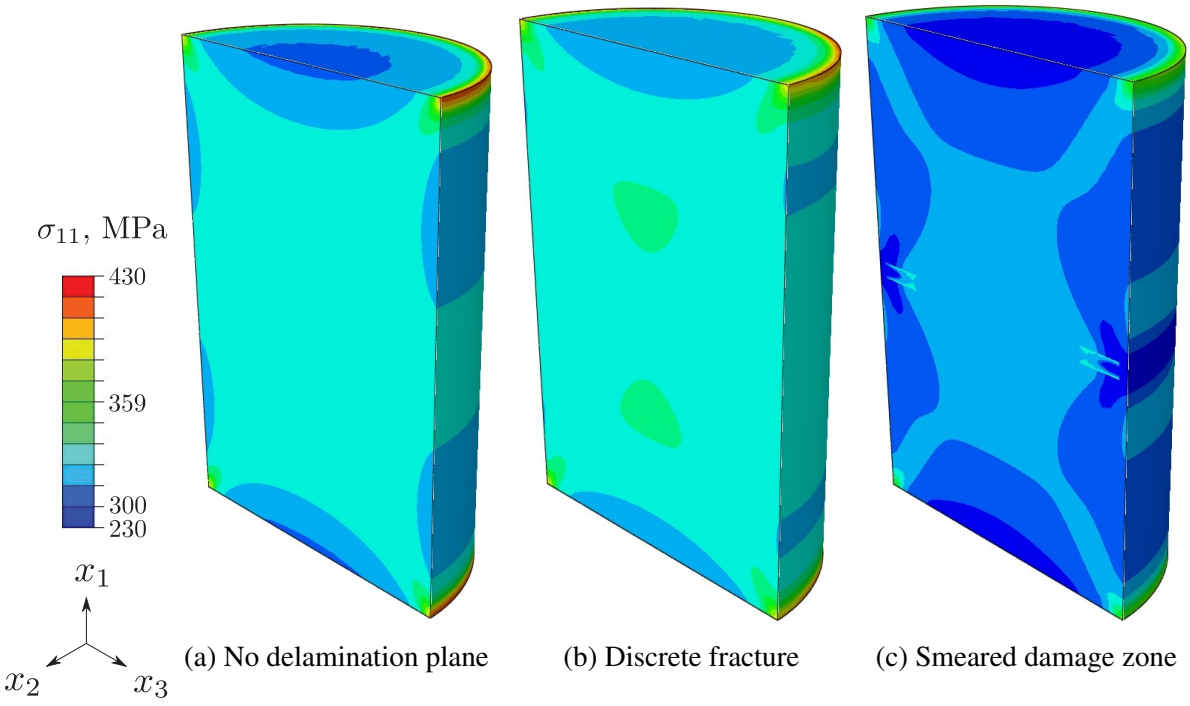

(a) No delamination plane (b) Discrete fracture (c) Smeared damage zone

FIG. 22: Comparison of the vertical stress distribution in the core sample with a linear elastic model, with a discrete fracture and with a smeared damage zone.

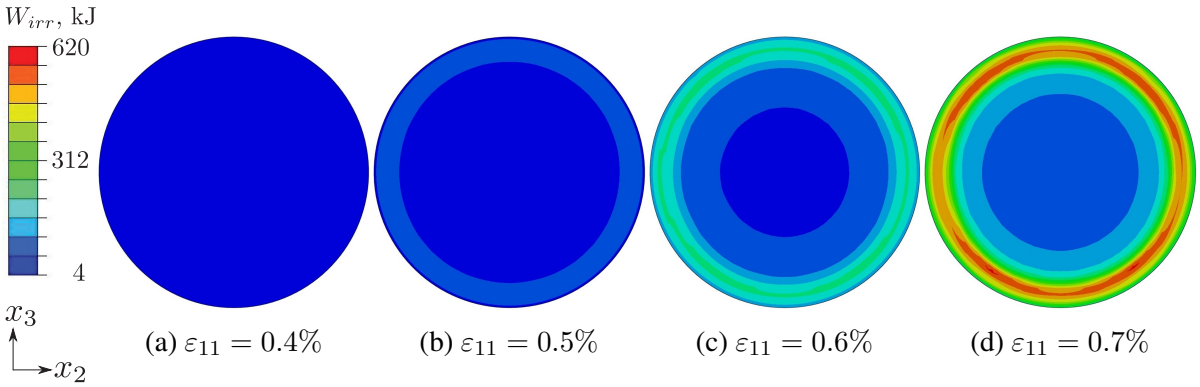

FIG. 23: Energy dissipated in the smeared damage zone due to crack opening (accumulation of irreversible strain $\boldsymbol{\varepsilon}^{id}$).

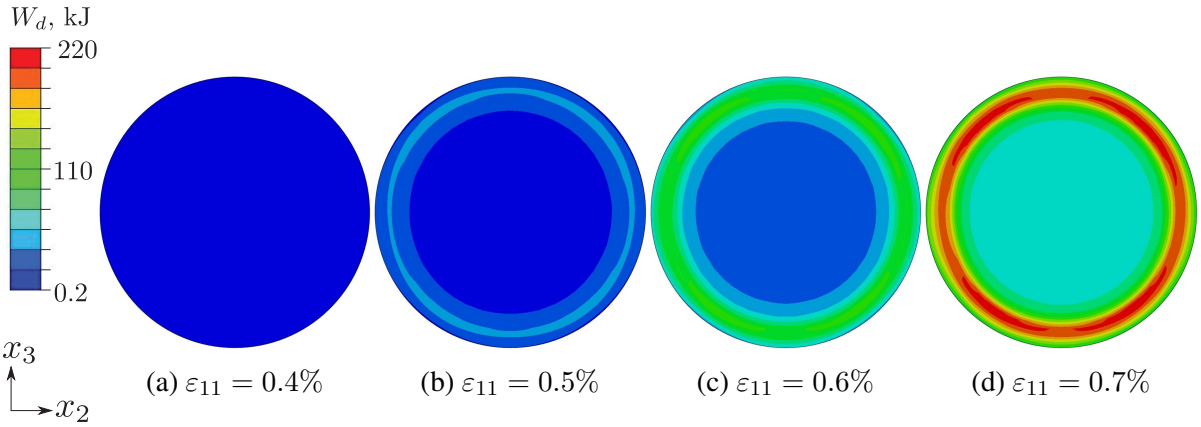

(a) $\varepsilon_{11} = 0.4\%$ (b) $\varepsilon_{11} = 0.5\%$ (c) $\varepsilon_{11} = 0.6\%$ (d) $\varepsilon_{11} = 0.7\%$

FIG. 24: Energy dissipated in the smeared damaged zone due to crack debonding (accumulation of damage $\boldsymbol{\Omega}$).